ACCSCIENCE PUBLISHING

International Journal of Bioprinting

RESEARCH ARTICLE

A 3D-bioprinted alginate-MgP scaffold for superior regeneration of calvarial bone defects in a rat model

Shaimaa ElShebiney[1], Sara A. M. El-Sayed[2], Mduduzi N. Sithole[3], Mashudu T. Mphaphuli[3], Hanan H. Beherei[2], Pradeep Kumar[3], Mostafa Mabrouk[2]*, and Yahya E. Choonara[3]*

[1]Narcotics, Ergogenics, and Poisons Department, Medical Research and Clinical Studies Institute, National Research Centre (NRC), Giza, Egypt

[2]Refractories, Ceramics and Building Materials Department, National Research Centre, Dokki, Cairo, Egypt

[3]Wits Advanced Drug Delivery Platform Research Unit, Department of Pharmacy and Pharmacology, School of Therapeutic Sciences, Faculty of Health Sciences, University of the Witwatersrand, Johannesburg, South Africa

(This article belongs to the *Special Issue*: *Multifunctional Bioprinting for Tissue/Organ Engineering*)

Abstract

While autologous transplants are the traditional standard intervention for non-healing bone defect regeneration, they carry many risks and limitations. Regenerative composite biomaterials are promising alternatives to conventional autograft and allograft implants. This study aimed to overcome these challenges by creating a novel biodegradable 3D biomaterial scaffold that mimics the structural and physiological properties of native bone. Scaffolds composed of magnesium phosphate (MgP) doped with copper oxide (CuO) in specific proportions (3, 5, or 7% [w/w]) were homogenously distributed in an alginate polymer matrix for the repair of calvarial bone defects in a rat model. The scaffolds were fabricated using a 3D bioprinting technique, and their physical properties were characterized through X-ray diffraction, Fourier transform infrared spectroscopy, and mechanical strength assessments. The bioactivity of the scaffolds was evaluated *in vitro* for biomineralization and cytotoxicity, revealing high biomineralization and cell viability. Female rats were used for the *in vivo* experiments, and the defects were examined using microscopic and histological analysis, computed tomography imaging, as well as serum markers including osteocalcin and procollagen III. The *in vivo* results demonstrated high efficacy of the scaffolds in promoting bone regeneration and enhanced healing in the calvarial defect model. The incorporation of CuO not only improved the scaffolds' mechanical properties but also exhibited angiogenic effects, fostering an environment conducive to bone healing. Our results indicated that the Alg–MgP–CuO scaffolds have great promise for bone tissue engineering applications and repair, especially with 7% (w/w) CuO doping.

***Keywords*:** 3D bioprinting; Alginate; Bone regeneration; Copper oxide doping; Magnesium phosphate.

***Corresponding authors:**
Yahya Choonara
(yahya.choonara@wits.ac.za)

Mostafa Mabrouk
(mostafamabrouk.nrc@gmail.com)

Citation: ElShebiney S, El-Sayed SAM, Sithole MN, *et al*. A 3D-bioprinted alginate-MgP scaffold for superior regeneration of calvarial bone defects in a rat model. *Int J Bioprint*. 2025;11(6):238-259. doi: 10.36922/IJB025190188

Received: May 9, 2025
1st revised: June 10, 2025
2nd revised: June 27, 2025
Accepted: July 2, 2025
Published online: July 2, 2025

1. Introduction

Bone defects or fractures, including congenital defects and osteoporosis, are common disability-linked health problems that impact the well-being of the population and standard of living. Traditional interventions—such as autograft, allograft, and xenograft—have demonstrated clinical success in many cases. However, several limitations remain, such as insufficient donor sites, risk of disease transmission,[1] high cost that may be unaffordable to many patients, and potential site morbidity or rejection.[2] Consequently, considerable research efforts have been directed toward developing artificial bone matrix using various materials—such as polymers, ceramics, metals—as well as mesenchymal cells and growth factors, to restore damaged osseous tissue. More recently, degradable metals, particularly iron (Fe)-based alloys, have received great attention as load-bearing scaffold substrates. For example, chloride-mediated dissolution and intrusion products have been demonstrated to persistently accelerate the degradation of Fe-based implants, and the preferential corrosion of secondary manganese-sulfide (Mn-S) phases markedly enhances the biodegradation of Fe–Mn-S biocomposites.[3,4] As bone defect issues become increasingly prevalent due to various factors—such as aging and lifestyle choices—there is an urgent need to innovate and improve biomaterials for effective and rapid bone repair.

There has been a marked increase in interest in employing 3D printing technologies for the fabrication of biomaterial scaffolds. Conventional engineering methods often fall short of addressing the complexities involved in bone regeneration, prompting extensive research into bioinspired materials that mimic natural bone. Bone scaffolds are biodegradable materials that are used to fill bone defects and act as an artificial extracellular matrix, supporting the proliferation and differentiation of host osteogenic cells until the native bone tissue and its biomechanical properties are fully restored.[5] An efficient 3D scaffold should be able to produce a similar composite to bone tissue, which is naturally built as a mesh of collagen fibers and hydroxyapatite crystals. The designers of these advanced 3D scaffolds aim to replicate the mechanical and osteoconductive properties that are crucial for effective bone healing.[6] Despite the progress, identifying and developing suitable composite biomaterials that can provide the necessary performance for bone tissue engineering (BTE) applications remains a significant challenge. The development of novel inks for 3D bioprinting is crucial, as it holds the potential to generate constructs that not only facilitate cell growth but also improve the overall regenerative capacity for treating large bone defects.

Various materials, including bioglass, hydroxyapatite,[7] tri-calcium phosphate,[8] polycaprolactone,[9] and polylactide-co-glycolide,[10,11] have demonstrated notable osteoinductive properties. Recently, magnesium phosphate (MgP) has gained significant attention due to its high *in vivo* solubility, which allows it to transform into calcium phosphate (CaP) phases under physiological conditions.[5]

The economic, safe, natural polymer alginate (Alg) is a perfect material for hosting cell regeneration, as it can serve as an extracellular matrix. The relative stability and biocompatibility of Alg make it suitable for use as a biomaterial.[12,13] Alg can produce stable hydrogels by interacting with bivalent ions (e.g., Mg) through its cation and carboxyl functional group. This crosslinking process renders the Alg hydrophobic, allowing it to be used for the fabrication of 3D scaffolds.[14,15]

From another perspective, the presence of antimicrobial agents such as copper (Cu) is essential for preventing secondary infections. Cu, a fundamental trace element associated with several physiological processes, is particularly valuable for hard tissue replacements and displays antibacterial and angiogenic capabilities, which favor osteogenesis.[16] This study proposes the development of a novel injectable ink for 3D bioprinting technology, which involves creating 3D biomaterial scaffolds from Alg–MgP-based composites with trace CuO doping through *in situ* conjugation using polyelectrolyte complexation. The ink could produce a 3D-printed composite scaffold that promotes bone growth with exceptional efficacy, building on previously established technologies. The prepared 3D scaffold was characterized using physicochemical, mechanical, and biomineralization assessments. Given the challenges associated with repairing large or irregular bone defects,[17] this study employed the rat calvarial critical-size defect model[17] to evaluate the *in vivo* bone-regenerative capacity of the 3D-printed scaffold.

2. Materials and methods

2.1. Materials

Ammonium dihydrogen phosphate ($NH_4H_2PO_4$; molecular weight: 115.03 g/mol) and magnesium nitrate hexahydrate ($Mg(NO_3)_2{\cdot}6H_2O$; molecular weight: 256.41 g/mol) were sourced from MERCk, Germany. Copper (II) nitrate trihydrate ($Cu(NO_3)_2{\cdot}3H_2O$; molecular weight: 241.60 g/mol) was sourced from QualiKems, India. Sodium Alg (molecular weight: 500,000 g/mol) was obtained from Kibun Food Chemipha, Japan Aldrich Chemical Co., Japan. Poly(ethyleneimine) solution (PEI; 50% [w/v] in water; molecular weight: 575,000) was acquired from Sigma-Aldrich (USA).

2.2. Preparation of CuO-doped MgP

We prepared a pure MgP sample at a ratio of 1:1 as previously reported.[17] Ammonium dihydrogen phosphate and magnesium nitrate hexahydrate were both dissolved in 400 mL of distilled water. The solution was then stirred for 1 h at room temperature with a magnetic stirrer and subsequently kept in the dryer at 80°C until gelation. The resulting hard gel was calcined at 600°C for 2 h. CuO-doped MgP samples were prepared using the same procedure, with copper (II) nitrate trihydrate incorporated in place of a corresponding proportion of magnesium. Three doping copper concentrations were prepared: 3, 5, and 7% (w/w) CuO. Comprehensive validation analyses of the obtained MgP nanopowders, both before and after CuO doping, have been previously reported.[17]

2.3. Bioprinted composite scaffold preparation

Sodium Alg (200 mg/mL) was dissolved in ultra-purified deionized water to form a bioink, which was then combined with pure MgP and CuO-doped MgP (200 mg/mL). Separately, 29% (v/v) PEI solution was prepared, with ethanol serving as the solvent. Using 3D Bioplotter® (EnvisionTEC, GmbH, Germany), Alg–MgP–CuO-doped scaffolds were constructed. The process was facilitated by computer-aided design software; 3D Bioplotter® software for scaffold construction and Visual Machine software for material and machine control. The printing parameters in this study were similar to those previously established by Sithole *et al.*[18] Prior to printing the 3D scaffolds, the viscosities of Alg solutions—in the presence and absence of different fillers— were measured using a digital viscometer (DAIHAN Scientific, South Korea). The device was calibrated according to the manufacturer's instructions prior to use. Samples were measured using spindle 4 at 6 rpm and at a constant temperature of 23°C to ensure accurate and consistent viscosity readings. The viscometer spindle was immersed in the sample to the required depth, and measurements were taken once the instrument reading stabilized to record the viscosity value. The scaffolds were fabricated at 37°C utilizing Alg–MgP–CuO-doped bioink supplied from a 30 cm^3 cartridge and extruded through a plastic nozzle (diameter: 0.41 mm) under a pressure of 0.5 bar, at a deposition rate of 8 mm/s, onto a Petri dish containing a solidifying solution of PEI dissolved in ethanol. The layers were deposited perpendicularly to the underlying layer, which was kept in PEI solution overnight to harden.

2.4. Scaffold characterization

2.4.1. X-ray diffraction

The crystallinity and amorphous characteristics of the Alg–MgP–CuO-doped 3D-bioprinted composite scaffolds were assessed using an X-ray diffractometer (RIGAKU, INC., Japan). The system was equipped with Cu-kα radiation (λ = 1.54056 Å). The samples were scanned over a 2θ range of 2–70° at 2°/min under ambient conditions.

2.4.2. Fourier transform infrared spectroscopy

Fourier transform infrared (FTIR) spectra of the 3D-printed scaffolds were obtained using an FTIR spectrophotometer (Perkin-Elmer, UK). High-resolution analysis was conducted over a wavelength range of 4000–650 cm^{-1}. The evaluation focused on determining the presence or absence of functional moieties in a 1–3 mg sample.

2.4.3. Texture analyzer for compressive strength measurement

The mechanical properties of the scaffolds were investigated using a texture analyzer (TA.XTplusStable Microsystems, UK). The tests were conducted on the 3D-printed scaffolds with dimensions of 10 × 10 × 10 mm^3. After the test, the scaffolds were allowed to return to their initial dimension.

2.4.4. Brunauer–Emmett–Teller surface area analysis

To evaluate the microstructural properties of the 3D-printed scaffolds, an N_2 adsorption/desorption analysis (ASAP 2000, Micromeritics Inc., USA) was performed. Samples were degassed under vacuum for 24 h at 40°C prior to measurements. The specific surface area of the 3D-printed scaffolds was assessed using the Brunauer–Emmett–Teller (BET) method.

2.5. Bioactivity of 3D-printed composite scaffolds

The 3D-printed scaffolds were submerged in 100 mL of simulated body fluid (SBF) for 14 days. At specific time intervals (1, 3, 7, and 14 days), 5 mL of the SBF was extracted to quantify ion release using a UV spectrophotometer, and the removed volume was replaced with fresh SBF. After 14 days, the 3D scaffolds were removed from the SBF solution, washed, and dried. The surface layer formed on the 3D scaffolds was then examined using scanning electron microscopy (SEM) combined with energy-dispersive X-ray spectroscopy (EDX; TESCAN, USA). The pH levels of the SBF solutions were measured at specified intervals during the incubation period. Additionally, the swelling capacity of 3D-printed scaffolds developed using Alg-based bioink was assessed.

2.6. Cell viability

Cell viability on 3D-printed scaffolds was evaluated using the human MG-63 cell line (PromoLab (Pty) T/A Separations, South Africa). The cells were cultured in Dulbecco's Modified Eagle Medium (Thermo Fisher Scientific, South Africa), supplemented with 10% fetal bovine serum, 2 mM L-glutamine, 1% penicillin G sodium, 1% streptomycin sulfate, and 250 ng/mL amphotericin B,

with the medium replaced every 3 days. The cytotoxicity of the scaffolds was assessed using an MTT assay. Briefly, the MG-63 cells were seeded in 48-well tissue culture plates at 1×10^5 cells per well in the presence of the 3D-printed scaffolds and incubated at 37°C in a humidified atmosphere with 5% CO_2. Evaluations were conducted at 24- and 48-h post-seeding. At the end of the incubation period, MTT solution (80 µL) was added to each well, and the cells were incubated for 4 h at 37°C. The formazan crystals were solubilized, and after 1 h, the absorbance at 570 nm was measured using a Victor™ X3 plate reader (PerkinElmer, Germany).

2.7. Mode of cell death

MG-63 cells were detected using fluorescent staining and incubated with the different scaffold composites (1 mg ± 10%) added to wells in duplicates for 24 and 48 h, as previously described.[19] A dual stain of acridine orange (100 µg/mL) and ethidium bromide (100 µg/mL) dissolved in phosphate buffer saline (PBS; Merck KGaA, Germany) was used, and the cells were evaluated under a fluorescence microscope (AxioImager Z2, Zeiss, Germany).

2.8. Alkaline phosphatase activity

To evaluate the effect of MgP within the Alg 3D-printed scaffolds on cell differentiation, alkaline phosphatase (ALP) activity was measured. Saos-2 cells were cultured in a serum-free media with 0.1% bovine serum albumin at a density of 5×10^4 cells per well and maintained at 37°C for 4 and 7 days. After incubation, the plate was washed with Hanks' balanced salt solution (HBSS, Sigma-Aldrich, USA). To lyse the cells, 80 mL of Triton® X-100 (0.5% in PBS) was added to each well. A 40 µL aliquot of lysate was collected from each well to evaluate ALP, and a 10 µL sample was used to determine protein concentration utilizing the BCA protein assay. ALP was quantified using p-nitrophenol,[5] and data were presented as µg of ALP per mg of total protein.

2.9. *In vivo* bone regeneration in rats with critical-size calvarial defects

2.9.1. Animals and surgical procedure

The study involved a total of 36 adult National Research Centre, Egypt (NRC)-inbred female Wistar rats, aged 12 weeks. The animals were kept in standard polyacrylic boxes and left to acclimatize for 1 week in the experimental room under controlled environmental conditions. All rats were randomly divided into six groups, including control, Alg, Alg–MgP, Alg–MgP–CuO3%, Alg–MgP–CuO5%, and Alg–MgP–CuO7%, according to the filling scaffold. The animals used as controls did not get any bone filler (3D scaffolds). The study was conducted in line with the Declaration of Helsinki and obtained approval from the Animal Care and Use Committee of the National Research Centre (approval no. 1311102022).

Rats were anesthetized with a ketamine/xylazine cocktail at doses of 70 and 7 mg/kg. The head was shaved and disinfected with alternative swabs of 70% ethanol and betadine. To expose the periosteum, a sagittal skin incision was performed, followed by a blunt dissection of the soft tissues. A circular bone defect was created using a 5-mm trephine drill under continuous irrigation with 0.9% saline to prevent local overheating. Scaffolds were then implanted into the defect region, either with Alg, Alg–MgP, Alg–MgP–CuO3%, Alg–MgP–CuO5%, or Alg–MgP–CuO7% scaffolds, or left unfilled for the control. The incision was sutured with nylon 10/0 sutures after the operation, followed by sanitization with betadine. Analgesic and 3 mL of saline were administered subcutaneously. A prophylactic intraperitoneal injection of antibiotics was delivered for 3 days following the surgical procedure. Computed tomography (CT) scans were performed in week 8. Blood samples were collected, and sera were separated. The animals were sacrificed, and the skulls containing the lesion were surgically removed and preserved in 15% formalin (formalin saline) for subsequent analysis.

2.9.2. Macroscopic evaluation

The skulls were defleshed after sacrifice, and the repaired defects were exposed and observed. The regenerative capacity was assessed utilizing an assessment scale established by Badawi *et al.*,[20] with scores ranging from 4 (minimal healing) to 11 (optimal recovery).

2.9.3. Computed tomography scan of rat calvaria

The samples were examined with a CT scanner (MRCE, Egypt). Specialized software was utilized to generate the volume of interest from the acquired 2D projections. Bone mineral density (BMD) was quantified as a metric for bone mineralization and was expressed in mg/cm³.

2.9.4. Histological examination and analysis

The specimens were decalcified with 10% ethylenediaminetetraacetic acid solution for 2 weeks, subsequently dehydrated by serial alcohol dilutions, and fixed in paraffin. The specimens were cut into 5 µm-thick sections and stained with haematoxylin and eosin. The prepared specimens were observed under light microscopy and recorded with a digital slide scanner. The resulting images were analyzed digitally using ImageJ 1.53e (National Institutes of Health, USA).

2.9.5. Bone turnover markers

Finally, sera were analyzed with ELISA commercial kits for procollagen-III (PIIINP) and osteocalcin, which are

markers of bone turnover. The results of these analyses were compared between the different groups.

2.10. Statistical analysis

In vitro data were statistically analyzed using two-way analysis of variance (ANOVA) with multiple comparisons. No statistically significant differences were observed between the samples at different time points when $p > 0.05$. Data from *in vivo* investigations are presented as mean ± standard deviation. Statistical analysis using one-way ANOVA was conducted for cell studies, with significance indicated at $p < 0.05$. The sample size was calculated using power analysis, allocating six animals to each group. All statistical analyses were performed using GraphPad Prism Version 10.2.0 (Graphstats Technologies, USA).

3. Results

3.1. Bioprinted composite scaffold development and characterization

Based on the viscosity measurements (Table 1), all scaffold solutions appear to fall within a range (0.3–600,000 P) suitable for extrusion-based 3D printing.[21]

3.2. XRD and FTIR analyses of the 3D-printed scaffolds

The X-ray diffraction (XRD) results (Figure 1) indicate several important findings regarding the scaffolds developed from MgP and CuO-doped nanopowders in the sodium Alg matrix. Firstly, the XRD curves of the composite scaffolds closely resemble those of pure MgP, and CuO-doping had minimal effect, suggesting that the crystalline structure of the nanopowders is preserved within the 3D-printed scaffolds. The structure of the MgP and CuO-doped MgP nanopowders appears to overlap over that of the Alg polymer. This indicates that the properties imparted by the nanopowders are more significant than those provided by the polymer alone, which is a common observation in similar studies involving bioactive materials. This behavior was commonly observed when bioactive semi-crystalline nanopowders were included in the polymeric matrix of 3D scaffolds.[22]

Table 1. Viscosities of scaffold solutions before 3D printing

Sample	Viscosity (P)
Alg	20.8 ± 0.6
Alg–MgP	25.9 ± 0.8
Alg–MgP–CuO3%	26.7 ± 0.5
Alg–MgP–CuO5%	29.5 ± 0.8
Alg–MgP–CuO7%	30.0 ± 0.7

The FTIR analysis of the developed scaffolds provides important insights into the chemical composition and interactions of the components involved. The spectra revealed several key functional groups that contribute to the overall properties of the scaffolds, which are critical for their application in tissue engineering. The presence of characteristic functional groups in the MgP nanopowders, such as the O–H groups, phosphate (PO_4^{3-}), and Mg–O bonds, is indicative of the materials' bioactive nature.[23,24] Broad absorption bands around 3448 cm^{-1} indicate water molecules essential for hydration and biological interactions (Figure 2A and B),[25] while a strong 1050 cm^{-1} P–O stretching band suggests potential for cell adhesion and proliferation.[26]

The FTIR spectra of MgP–CuO-doped scaffolds exhibited similar features to CuO-free MgP, indicating that doping did not significantly alter the material's fundamental structure (Figure 2B–D). However, a reduction in O–H bond intensity suggests the formation of Cu–O bonds, potentially affecting hydration and ion release. Peaks between 623–625 cm^{-1} corresponded to phosphate ion vibrations,[27] while Mg–O stretching bands (578–587 cm^{-1}) confirmed the presence of Mg.[28]

Sodium Alg was identified by a broad 3500–3000 cm^{-1} stretch, with 1595 and 1397 cm^{-1} peaks linked to carboxylate groups. PEI was confirmed by NH_2 stretching peaks at 3345 and 3287 cm^{-1} and CH_2 vibrations at 2945 and 2844 cm^{-1}, highlighting its role in mechanical stability and biocompatibility.[29,30] The interaction between MgP and the polymer matrix likely improves scaffold performance by preventing direct nanopowder-tissue contact, which may regulate ion release and minimize cytotoxicity.[31]

The incorporation of Cu ions into the MgP framework is anticipated to enhance the biological activity of the scaffolds. Cu is known to play a vital role in angiogenesis by stabilizing hypoxia-inducible factor, thereby promoting blood vessel formation crucial for tissue regeneration. The expectation that Cu ions will be released into the extracellular environment is significant, as it could facilitate enhanced angiogenic responses.

3.3. Compressive strength of the 3D-printed scaffolds

The mechanical resilience of the 3D-printed cubic scaffolds was determined using a texture analyzer. As displayed in Figure 3, the inclusion of MgP nanopowders with and without Cu significantly enhanced the mechanical stability of the engineered scaffolds. Specifically, nanopowder-free polymeric scaffolds exhibited a lower mechanical strength (11.82 MPa), while the presence of

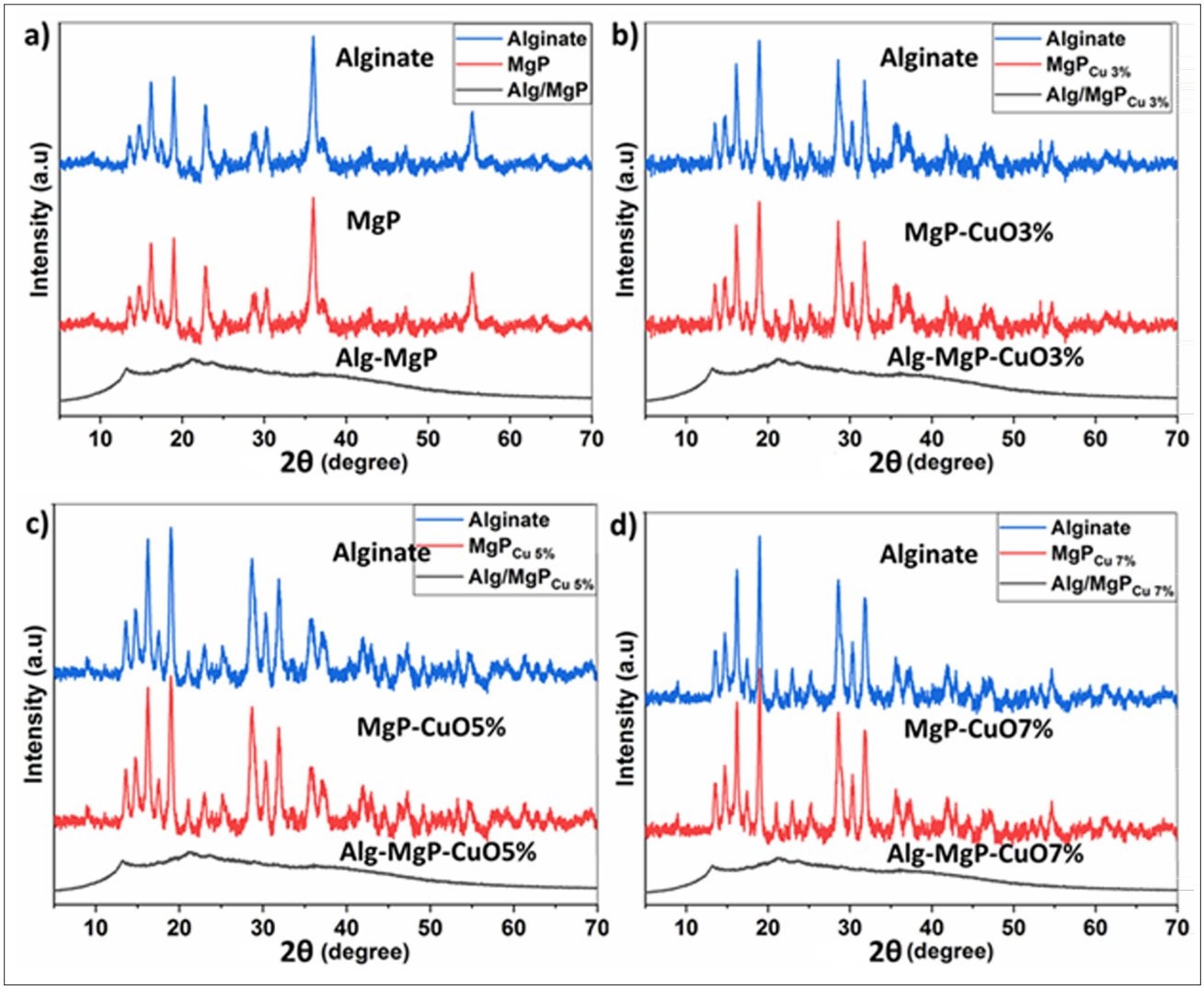

Figure 1. X-rays diffraction (XRD) curves of the 3D-printed composite (Alg–MgP–CuO-doped) scaffolds: Alg–MgP (a), Alg–MgP–CuO3% (b), Alg–MgP–CuO5% (c), and Alg–MgP–CuO7% (d).

MgP nanopowders increased the mechanical strength (30.27 MPa). Doping with Cu resulted in a notable increase in compressive strength (47.45 MPa). Previous studies have highlighted that the presence of transition metals in nanopowders contributes to the enhancement of mechanical properties.[30–33] However, the inclusion of inorganic nanopowders within the matrix of polymeric scaffolds facilitates the development of suitable implants for the repair of damaged hard tissues.[34]

3.4. Surface area of the 3D-printed scaffolds

Surface area and porosity analyses provided structural insights into the fabricated scaffolds, which can be correlated with potential biological applications. The porosity ratio—ratio between pore volume and solid volume—is critical for preserving the integrity of the scaffold after implantation and promoting nutrient diffusion and cell infiltration into the scaffold, both of which are essential for tissue regeneration.[35,36] Results demonstrated that the presence of MgP or CuO-doped nanopowders in the Alg matrix enhanced scaffold porosity, consistent with the observed increase in BET surface area across different compositions.

Figure 4 illustrates the adsorption isotherm of the fabricated scaffolds, comparing their behavior before and after the incorporation of MgP nanopowders into the Alg polymer matrix. Generally, the isotherm curves of all the scaffolds exhibited type IV and V classes. The presence of hysteresis loops (H3-type) as shown in Figure 4A and C, indicates loosely packed, plate-like particle aggregates, likely due to the MgP nanopowders.[37] This classification

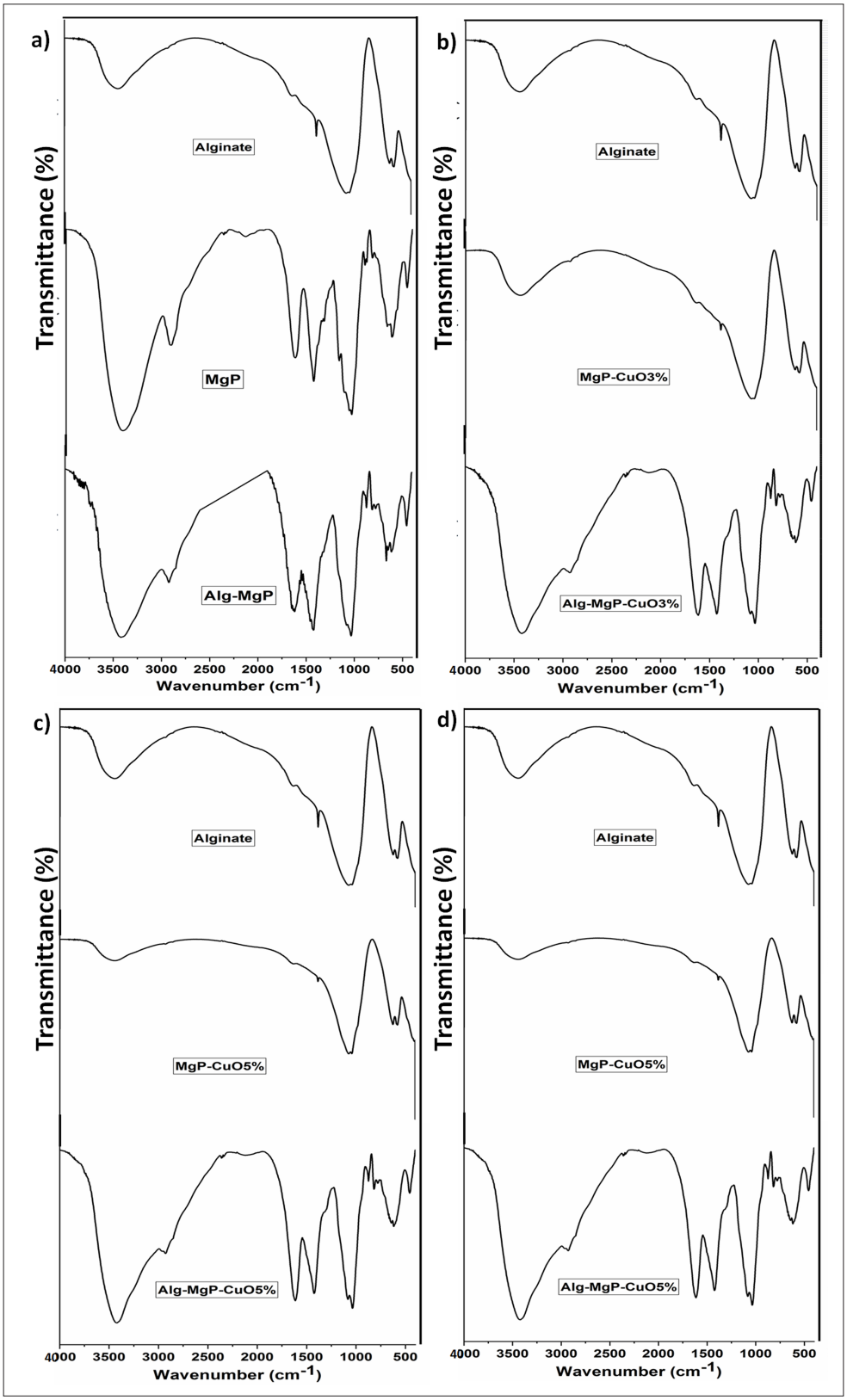

Figure 2. Fourier transform infrared spectroscopy (FTIR) spectra of the 3D-printed composite (Alg–MgP–CuO-doped) scaffolds: Alg–MgP (a), Alg–MgP–CuO3% (b), Alg–MgP–CuO5% (c), and Alg–MgP–CuO7% (d).

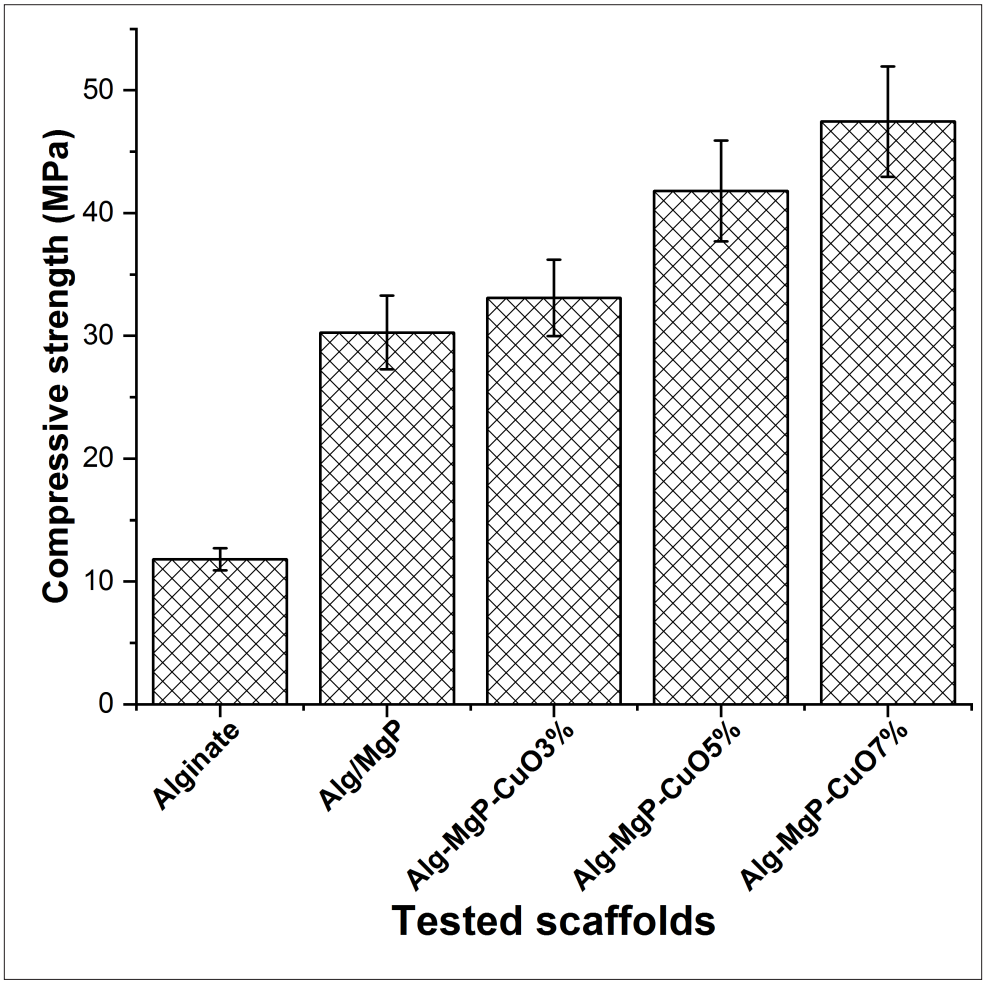

Figure 3. Compressive strength of the 3D-printed scaffolds (n = 3).

aligns with the expected behavior of scaffolds designed to mimic the extracellular matrix, as mesoporous structures are known to support cell adhesion and growth by providing a conducive microenvironment. The occurrence of non-closed desorption isotherms (Figure 4B and D), which is linked to the physical properties of the adsorbate rather than pore size, highlights the complexity of gas interactions within the scaffold's porous structure.[35,38]

The adsorption phase cavitations in the pores are responsible for the complexity of gas interactions within the scaffold's porous structure. Due to cavitation pressure effects, the pore size distribution is derived from the adsorption isotherm. While this peak is observed, it is important to note that it may not accurately reflect the functional pore sizes relevant for biological applications because it arises from cavitation phenomena associated with N_2 desorption at 77K. The findings demonstrate that the concentration of Cu ions in MgP-doped nanopowders increases the porous interface of the scaffolds. The measured surface area of the pure Alg, Alg–MgP–CuO3%, Alg–MgP–CuO5%, and Alg–MgP–CuO7% scaffolds were 0.379 ± 0.17, 1.635 ± 0.16, 3.369 ± 0.12, and 3.8 ± 0.13 m^2/g, respectively. This enhancement in porosity and surface area is significant, as a higher surface area can facilitate greater adsorption of biological molecules and improve the scaffolds' interaction with surrounding tissues. The increased surface area suggests that the scaffolds may provide more active sites for cellular attachment and growth, thereby enhancing their bioactivity.

3.5. Surface morphological changes of the 3D-printed scaffolds

Figure 5 displays the SEM images used to evaluate the effect of Cu on the formation of CaP layers on the surface of the 3D-printed scaffolds. The concentration of Cu was found to affect the quantity, size, and shape of the CaP layer. The EDX analysis revealed that the 5% CuO-doped

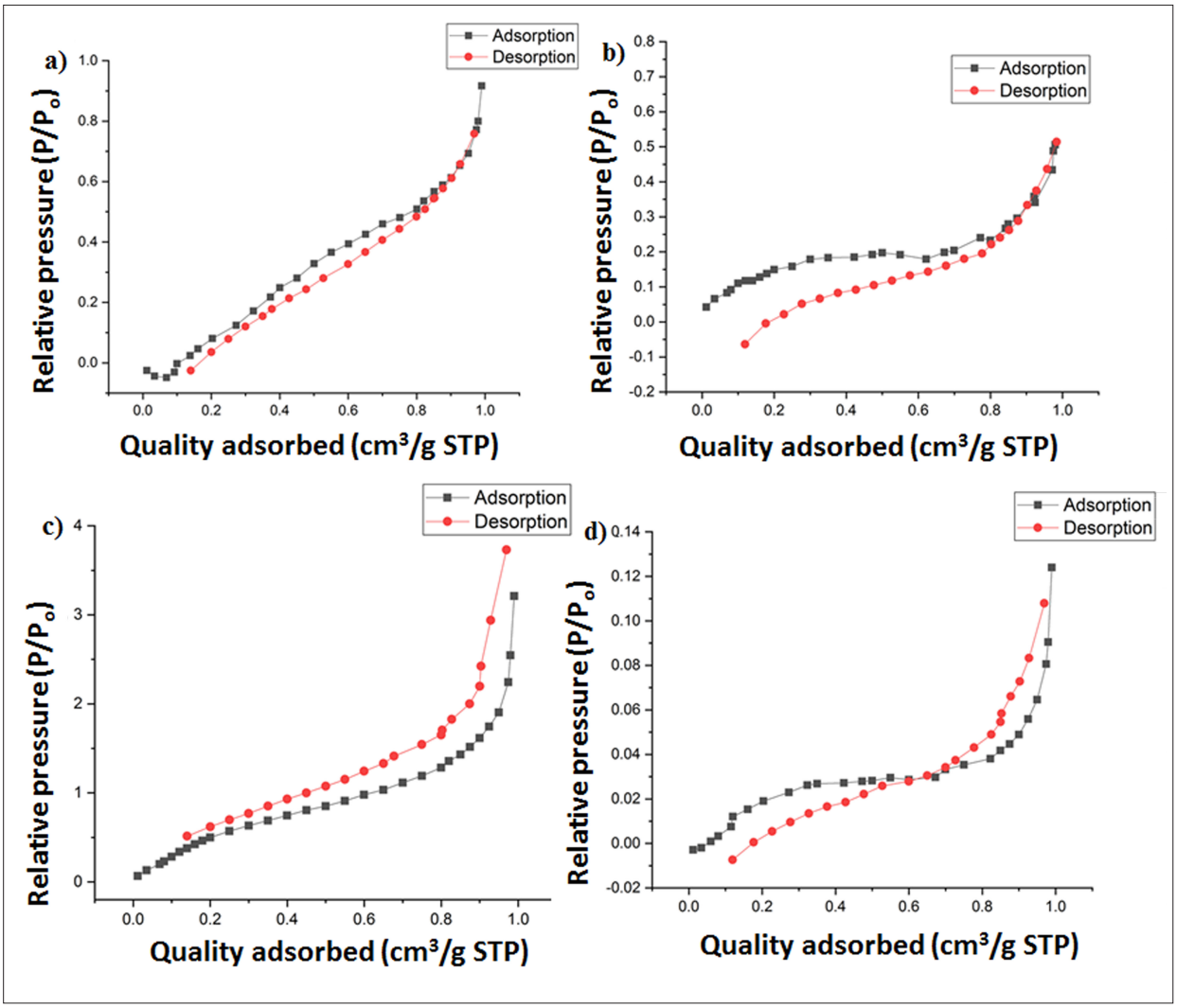

Figure 4. Isotherm curves of the fabricated scaffolds obtained by BET surface area measurements: (a) Alg–MgP, (b) Alg–MgP–CuO3%, (c) Alg–MgP–CuO5% and (d) Alg–MgP–CuO7%. Abbreviations: BET, Brunauer–Emmett–Teller; STP, standard temperature and pressure.

scaffold exhibited the highest calcium-to-phosphorus ratio, closely resembling that of hydroxyapatite. This observation is consistent with previous research that highlighted the positive impact of Cu presence on hydroxyapatite formation.[17,39–41]

3.6. Bioactivity of the 3D-printed scaffolds

Ion release from the 3D-printed scaffolds in the SBF (P, Ca, and Mg) and pH changes were measured over 14 and 28 days, respectively (Figure 6). The release of P ions decreased in the first 3 days of immersion due to swelling of the 3D scaffolds; the incorporation of MgP initiated the release of P ions, thereby restoring the original concentration. In contrast, Ca ions increased in the initial phase, especially in CuO-doped scaffold solutions; Ca ion release increased gradually until day 5, then decreased until day 14. The decrease in P and Ca ion concentrations at these time points suggests a correlation to the deposition of a mineralized layer on the scaffold surface.

On day 1, the Mg ion concentration in the SBF containing the 3D scaffolds decreased due to water absorption or the uptake of the solution by the MgP bioactive glass. From day 2, Mg ion concentration gradually increased until day 14, and this can be attributed to their release from the MgP scaffold. However, the concentration of Mg ions after 14 days was relatively low compared to its initial concentration in the SBF. Variations in pH of the SBF throughout the immersion period are parallel to the release and deposition of Ca and P ions (Figure 6D). Due to the alkaline nature of Ca ions and the acidic nature of

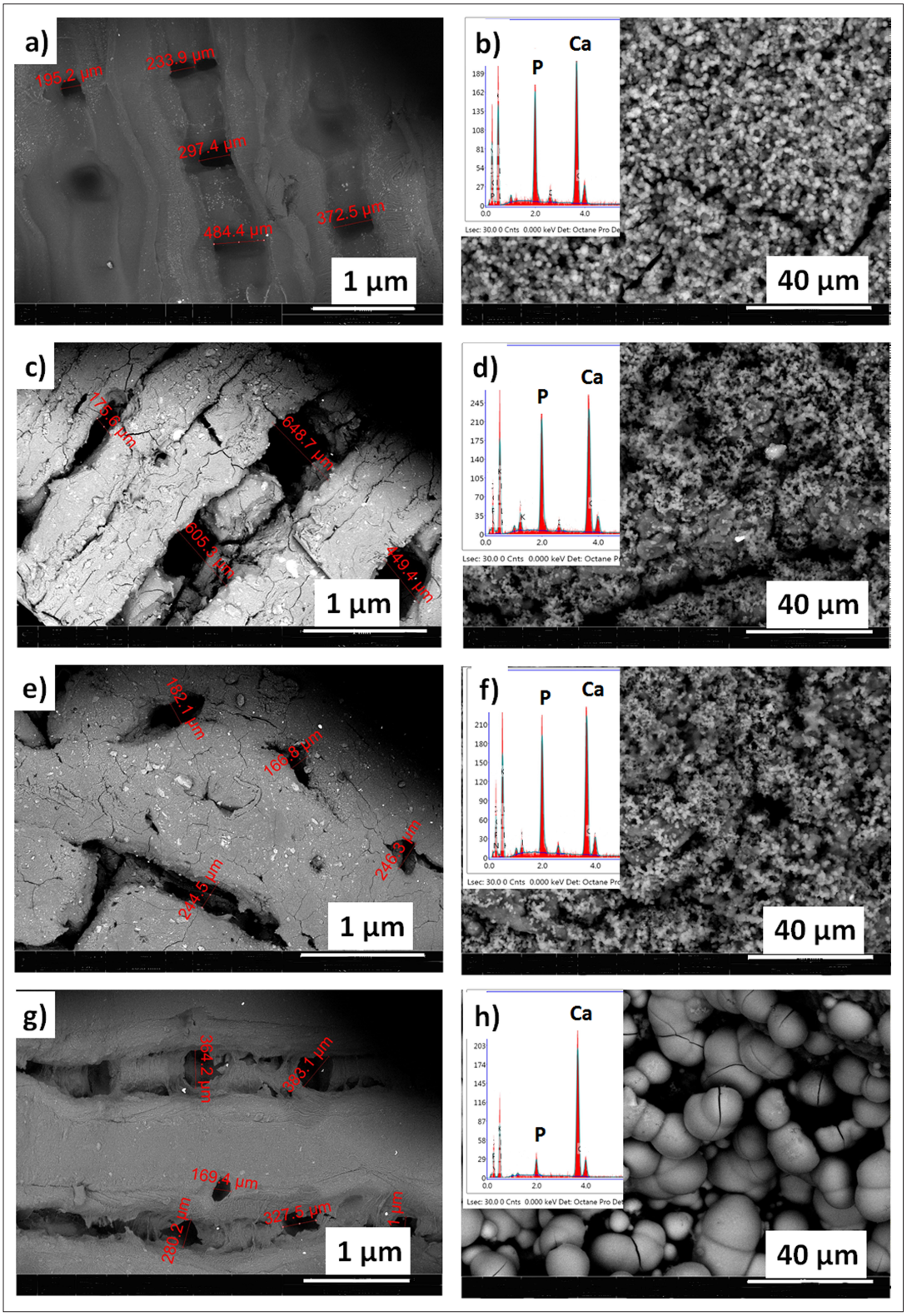

Figure 5. Scanning electron microscopy (SEM) images of the 3D-printed scaffolds. SEM images (a, c, e, and g) of the 3D-printed scaffolds before soaking in SBF: (a) alginate, (c) Alg–MgP, (e) Alg–MgP–CuO3%, and (g) Alg–MgP–CuO7%. SEM images (b, d, f, and h) and energy dispersive X-rays (EDX) analyses (inset) of the 3D-printed scaffolds after immersion in SBF: (b) alginate, (d) Alg–MgP, (f) Alg–MgP–CuO3%, and (h) Alg–MgP–CuO7%. Scale bars: 1 µm (a, c, e and g); 40 µm (b, d, f and h). Abbreviations: P, phosphorus; Ca, calcium; Lsec: Low secondary electrons; Det: Detector.

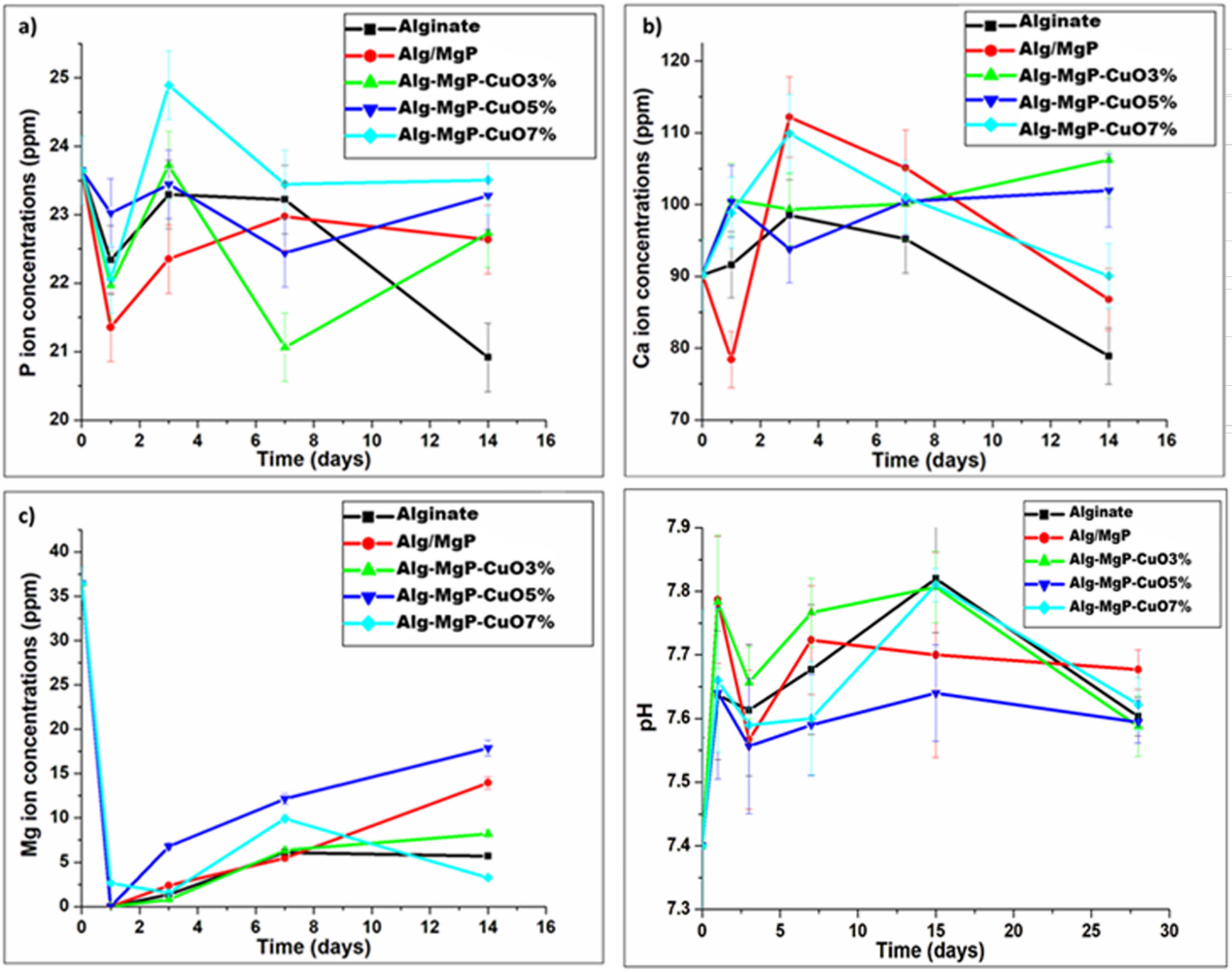

Figure 6. Ion release from the 3D-printed scaffolds and pH changes in the simulated body fluid (SBF). Concentrations of ions in the SBF over 14 days: (a) P, (b) Ca, and (c) Mg ($n = 3$). (d) Changes in pH over 28 days ($n = 3$). Abbreviations: P, phosphorus; Ca, calcium; Mg, magnesium; ppm: particle per million.

P ions, the pH value increased during the first 3 days as the concentration of Ca ions increased while that of P ions decreased. However, as the P ions increased after 5 days, the pH value subsequently decreased.

Figure 7 displays the percentage of swelling that occurred in the 3D-printed scaffolds over 28 days. The swelling percentage progressively increased for 3 days, followed by a decline. This was caused by potential interactions between the scaffolds and the SBF, such as ion release from the scaffolds into the SBF solution. The results highlighted distinct behaviors at specific time points: Alg (5% at day 1, peaking at 20% on day 15, 18% at day 28); Alg/MgP (10% on day 1, peaking at 45% on day 15, 40% at day 28); Alg–MgP–CuO3% (8–35%); Alg–MgP–CuO5% (7–30%); and Alg–MgP–CuO7% (6–28%). The high solubility of MgP led to the Alg/MgP scaffold exhibiting the greatest swelling, whereas the CuO-doped scaffolds displayed lower swelling percentages, presumably due to the increased mechanical strength and stability imparted by CuO-doping. At day 28, all scaffolds exhibited a decline in swelling, suggesting a stabilization of their structure. Nonetheless, the Alg/MgP scaffold exhibited the highest swelling percentage (i.e., 40%). These swelling behaviors can be attributed to the unique properties of the scaffold materials, particularly the high solubility of MgP and the mechanical enhancements imparted by Cu. Due to the high solubility of MgP, the Alg/MgP scaffold exhibited the highest swelling percentage.[41] However, the incorporation of Cu enhanced the mechanical strength and chemical stability of MgP, resulting in reduced swelling in the Cu-doped scaffolds.[42]

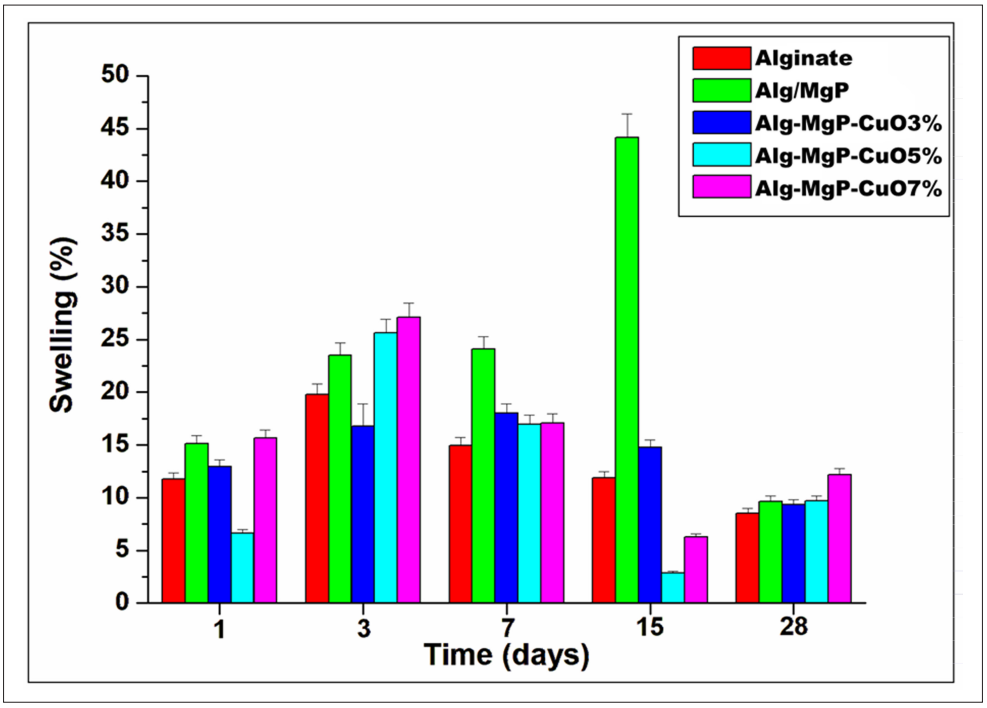

Figure 7. Swelling percentage of the 3D-printed scaffolds (n = 3).

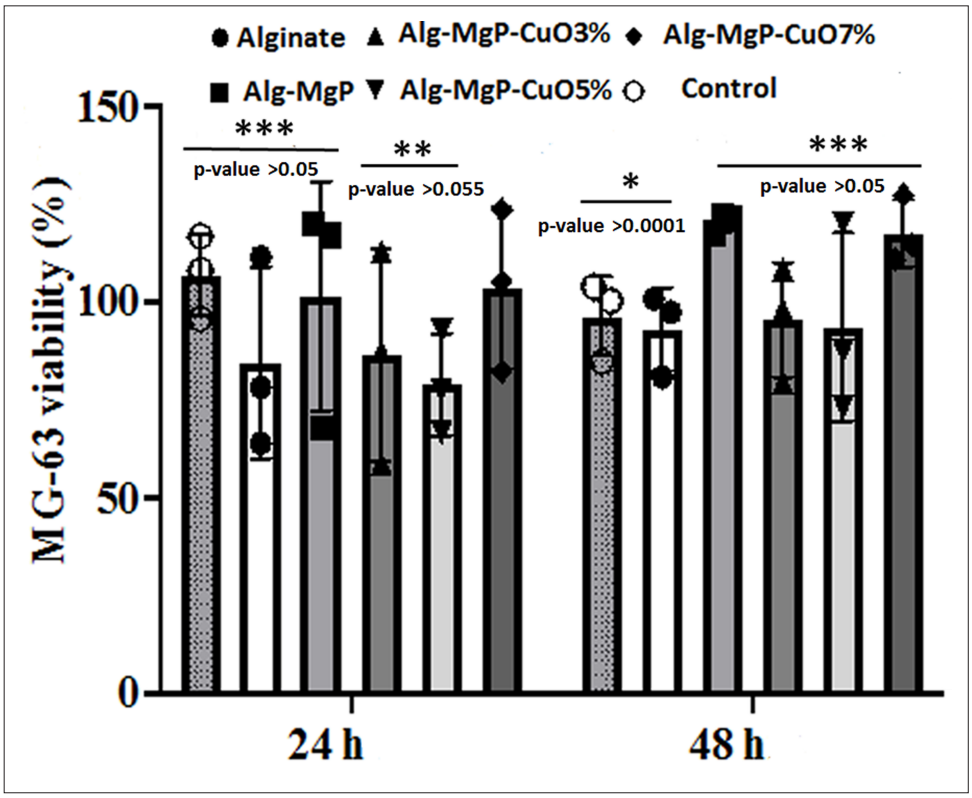

Figure 8. Cell viability of the different scaffolds (n = 3). Two-way analysis of variance (ANOVA) with multiple comparisons displayed no significant differences between samples at different time points ($p > 0.05$). * represents groups that are statistically similar to each other. ** indicates a different statistical grouping from *. *** further differentiates another set of groups that might show significant differences in cell viability compared to both * and **.

The significant increase in swelling for the Alg–MgP scaffold can be attributed to its interaction with the SBF. The high solubility of MgP facilitates the release of ions into the SBF, contributing to the initial increase in swelling by promoting osmotic pressure within the scaffold. Consequently, the Alg–MgP scaffold exhibited the highest swelling percentage among the scaffolds tested. However, after 3 days, a decline in swelling was observed, suggesting that while the initial hydration promotes swelling, the mechanical integrity of the scaffold is crucial in limiting excessive expansion.[6,13,15] The incorporation of Cu into the scaffolds mitigates this excessive swelling due to its role in enhancing mechanical strength and chemical stability, which is vital for maintaining scaffold shape and function during tissue engineering applications.[16,42] Notably, the swelling behavior of the Alg–MgP scaffold illustrates the significance of material composition in regulating hydration and stability.

3.7. Cytotoxicity of the 3D-printed scaffolds

The cell viability of MG-63 cells cultured on the 3D-printed scaffolds was evaluated (Figures 8 and 9). The scaffolds demonstrated cell viability comparable to the control (unexposed cells). However, 7% CuO-doped scaffolds displayed a relative increase in cell viability, likely due to the leaching of alkaline particles in the culture media, which has a positive effect on cell viability. These results were also confirmed by ALP activity analysis (Figure 10),

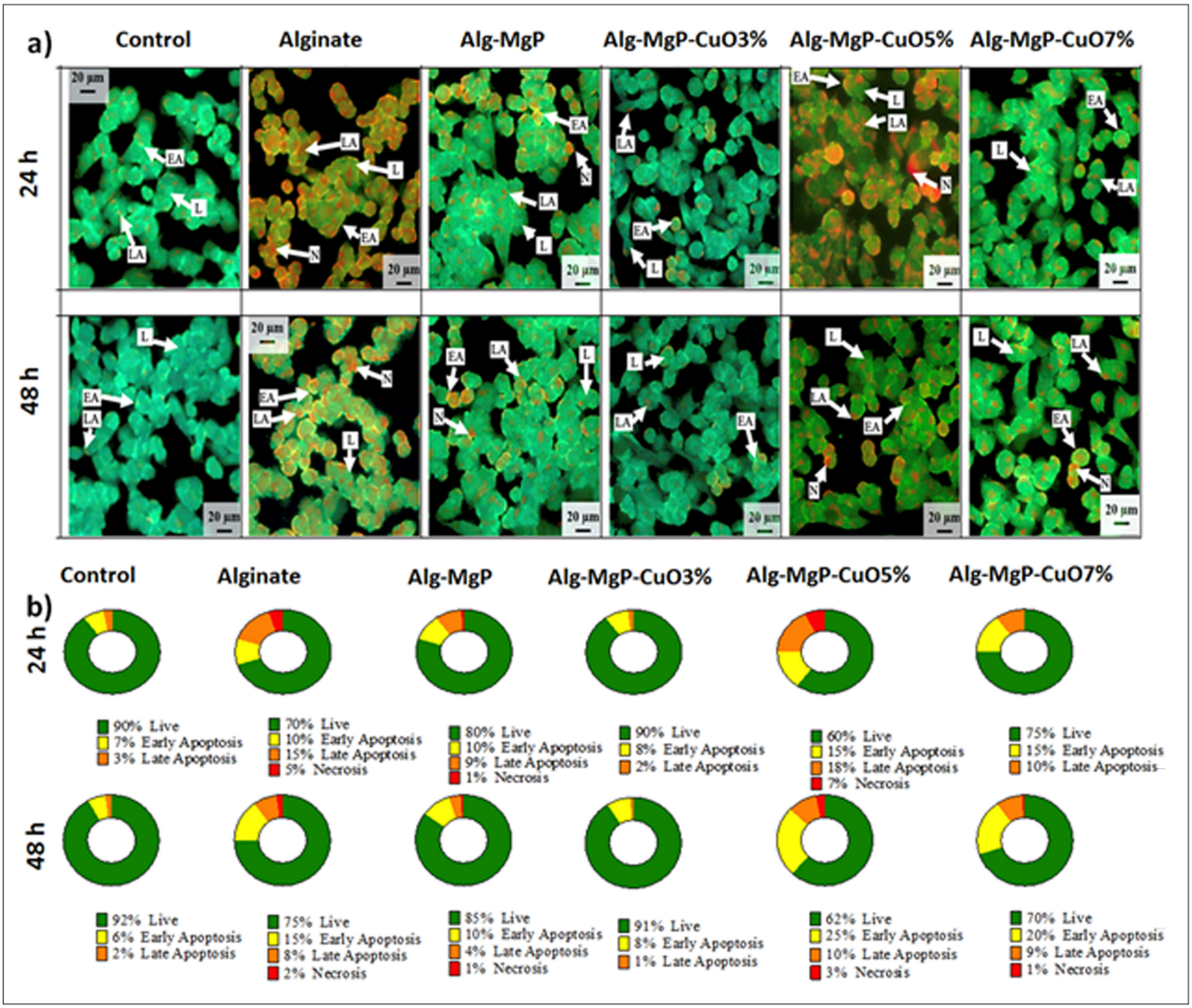

Figure 9. Cell viability of MG-63 cells cultured on the 3D-printed scaffolds. (a) Fluorescent microscopy images depicting live and apoptotic cells in the control and experimental groups at 24 and 48 h. Magnification: 20×. Scale bars: 20 µm. (b) Percentage of live, early apoptotic, and necrotic cells, illustrating the effects of different treatments on cell viability. Abbreviations: EA, early apoptosis; L, live; LA, late apoptosis; N, necrosis.

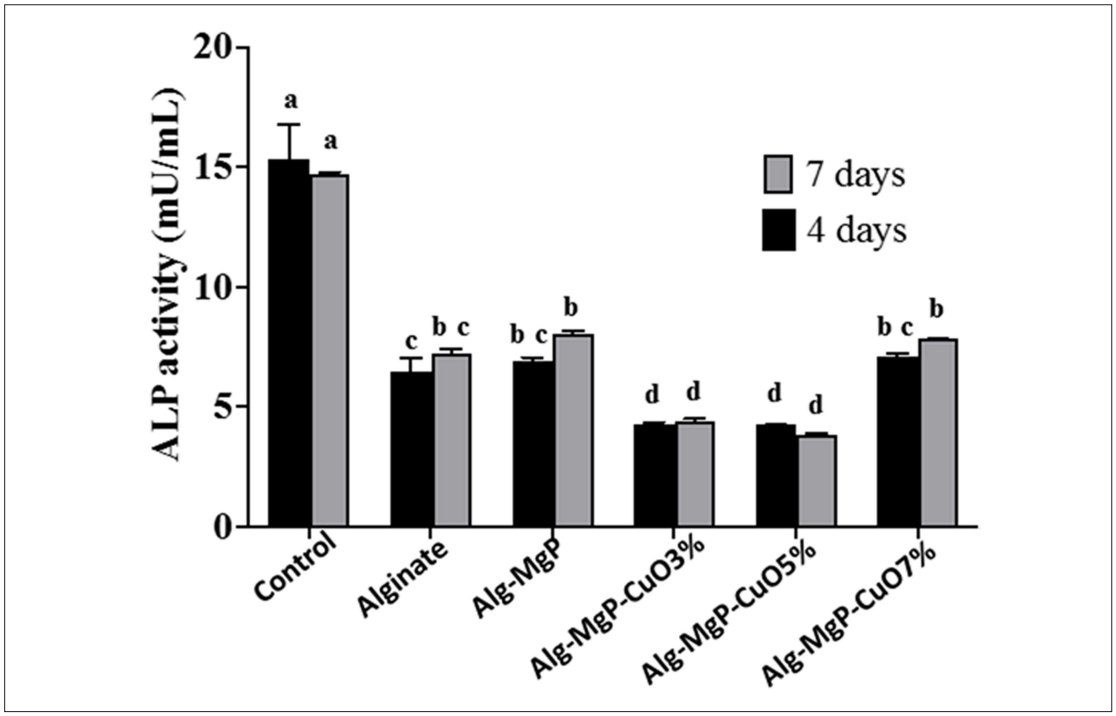

Figure 10. Alkaline phosphatase (ALP) activity in all scaffolds on days 4 and 7. Bars denoted with the same letters indicate no significant difference. Two-way analysis of variance (ANOVA) with multiple comparisons displayed no significant differences between samples at different time points ($p > 0.05$). "a" represents groups that are statistically similar to each other ($p > 0.005$). "b" indicates a different statistical grouping from "a" ($p > 0.01$). "c" further differentiates another set of groups that might have significant differences in ALP activity compared to both "a" and "b" ($p > 0.05$). "d" represents groups that are distinct from those labeled "a," "b," and "c" ($p > 0.001$).

where all scaffolds reported significantly lower ALP activity compared to the control ($p < 0.001$). For each scaffold type, no significant difference in ALP activity was observed between days 4 and 7 ($p > 0.05$). ALP activities of Alg–MgP–CuO3% and Alg–MgP–CuO5% were significantly lower compared to the other scaffolds ($p < 0.001$).

3.8. *In vivo* evaluation using a rat calvarial critical-size defect

3.8.1. Macroscopic evaluation

The calvarial defect model is commonly used to evaluate the bone regeneration potential of biomaterials.[21] This model is suitable for studying fractures in flat bones, such as those of the skull, ribs, and pelvis. The results revealed that all defect sites healed adequately, with no notable indications of infection or inflammation. The data demonstrated the distinct efficacy of CuO-doped MgP in promoting calvarial defect repair in the animal model. The median scores were: 4.5 (coefficient of variation [CV]: 17%) for the control group, 4.0 (CV: 9.8%) for Alg scaffolds, 5.5 (CV: 14%) for Alg–MgP scaffolds, 8.0 (CV: 16%) for Alg–MgP–CuO3% scaffolds, 9.5 (CV: 8.4%) for Alg–MgP–CuO5% scaffolds, and 12 (CV: 4.4%) for Alg–MgP–CuO7% scaffolds. The scores for both Alg–MgP–CuO5% and Alg–MgP–CuO7% scaffolds were significantly higher compared to the control group ($p < 0.05$).

3.8.2. CT scan of the calvarial defect

The CT scan displayed complete ossification of the defects in rats filled with Alg–MgP–CuO7%, while the control rats had an exposed defect (Figure 12). Alg and Alg–MgP scaffolds revealed narrowing of the defect by 20%, whereas Alg–MgP–CuO3% and Alg–MgP–CuO5% displayed over 50% defect filling, consistent with previous reported outcomes for bone implants.[27,43,44,45] There was no significant difference in BMD between defects filled with Alg or Alg–MgP and the control group ($p > 0.05$). Incorporation of CuO significantly increased the BMD ($p < 0.05$). Alg–MgPCu–O7% defect filling was significantly higher compared to Alg–MgP–CuO3% and Alg–MgP–CuO5% ($p < 0.05$) (Figure 12).

3.8.3. Serum procollagen-III and osteocalcin levels

Osteocalcin level was significantly higher after implantation with Alg–MgP–CuO5% and Alg–MgP–CuO7% compared to the control and Alg scaffolds ($p < 0.05$) (Figure 13A). Likewise, the serum PIIINP level significantly increased in the Alg–MgP–CuO7% scaffold group compared to the

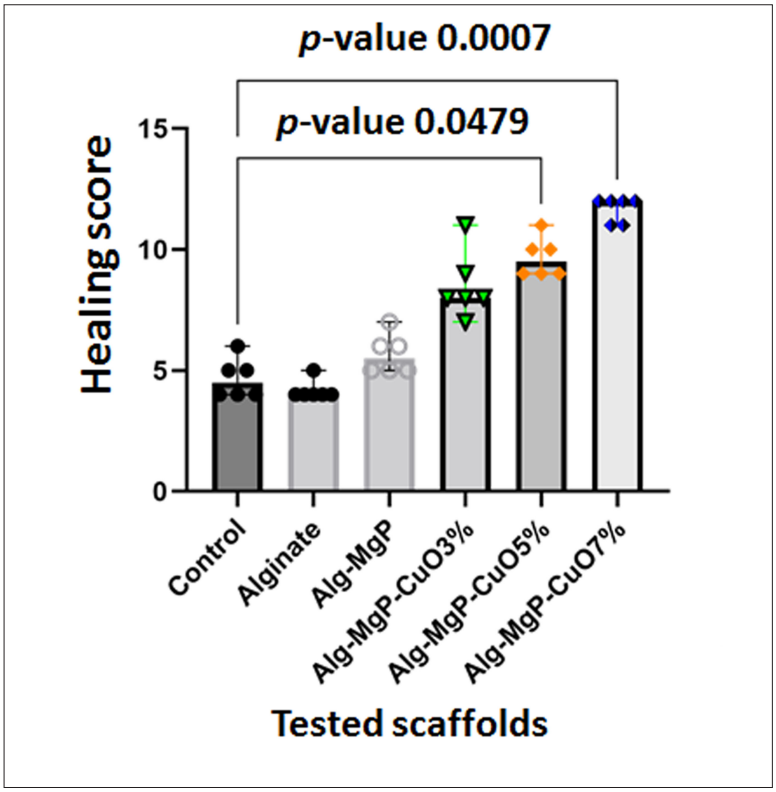

Figure 11. Healing score of the implanted 3D scaffolds (n = 3).

other scaffold and control groups (Figure 13B), consistent with the healing scores presented in Figure 11.

3.8.4. Histological assessment

Control animals with unfilled defects revealed granulation tissue, new blood vessels, and fibrous tissue, while Alg scaffold-filled defects displayed regenerated bone at the boundary of the defect with some scattered blood vessels. Alg–MgP-filled scaffold revealed fibrous tissue and scattered cartilage. CuO-doped scaffolds exhibited enhanced angiogenesis. Bone defects treated with 3% CuO revealed regeneration at the defect boundary and within the defect area, along with multiple scattered blood vessels. The 5% CuO scaffold yielded comparable results to the 3% CuO scaffold. In contrast, bone defects treated with 7% CuO scaffold demonstrated regeneration around the defect perimeter, characterized by fibrous tissue and highly vascular tissue (Figure 14).

4. Discussion

In this study, we developed a bioink for 3D printing bone grafts composed of Alg and MgP composites. This study is the first to utilize MgP-based bioink containing CuO as a dopant in BTE. The viscosity of a bioink is a critical factor in determining its printability, as it influences flow through the nozzle, layer adhesion, and the shape fidelity of the final structure. The ideal viscosity range depends on the specific 3D printing technique used, with extrusion-based printing accommodating a broader range compared to droplet-based methods.[21] Results from the XRD and FTIR analyses provide important insights into the structural integrity and chemical composition of the developed 3D scaffolds. Despite the presence of CuO, the XRD patterns indicate that the crystal structure of MgP remains unchanged.[22–30] CuO doping was confirmed to enhance the mechanical properties and biocompatibility of the 3D-printed scaffolds. The increased compressive strength reflects improved structural integrity and facilitates the transfer of the nanopowder's properties to the final scaffold structure, surpassing those of the Alg matrix alone. However, the complete incorporation of MgP and CuO-doped MgP nanopowders into the Alg matrix highlights the crucial role of polymers as support materials. FTIR analysis supports these findings by revealing key chemical groups associated with the scaffold's bioactivity. The characteristic O–H and P–O bonds suggest that the scaffold can facilitate cell adhesion and spreading,[35–38] which are essential for successful tissue engineering. The presence of CuO within

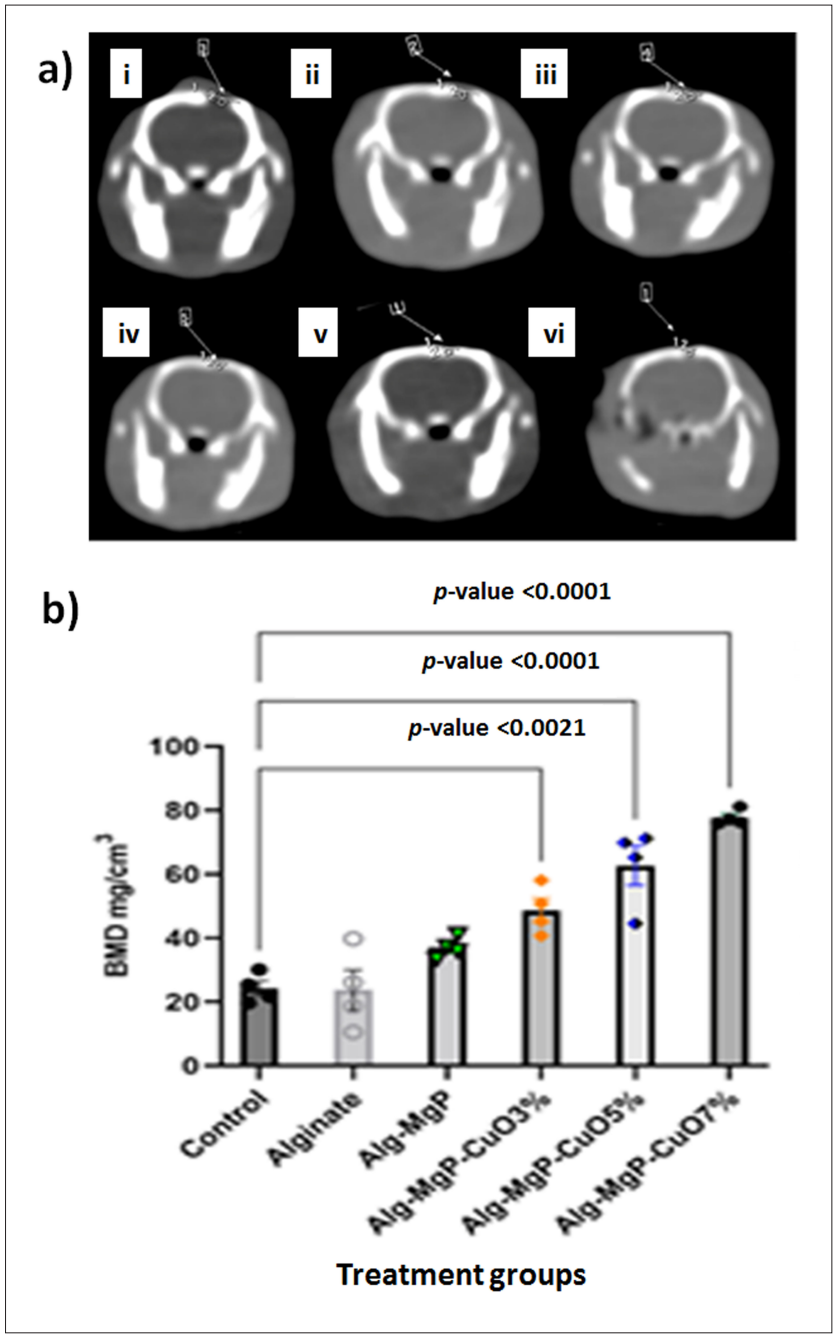

Figure 12. Effect of the implanted 3D scaffolds on ossification in rats suffering from calvarial bone defect. (a) Computed tomography (CT) images of the calvarial bone defect in different groups: (i) control, (ii) alginate, (iii) Alg–MgP, (iv) Alg–MgP–CuO3%, (v) Alg–MgP–CuO5%, and (vi) Alg–MgP–CuO7%. (b) Bone mineral density (BMD) of the implanted 3D scaffolds ($n = 3$). Data is presented as the mean ± standard deviation; data were analyzed using one-way analysis of variance (ANOVA), with statistical significance set at $p < 0.05$.

the 3D scaffold matrix decreases the vibrational intensity of the O–H groups, suggesting the formation of Cu–O bonds. These bonds may alter the hydration dynamics and ion release behavior, potentially enhancing the biological activity of the scaffolds.[38–42]

Commercial synthetic bone grafts primarily rely on CaP or other minerals. Moreover, most available commercial products, including Bioresorb, Chronos, Norian SRS, Ostim, and Vitos, are not produced in a 3D format; instead, they are either available in the form of granules or injectable

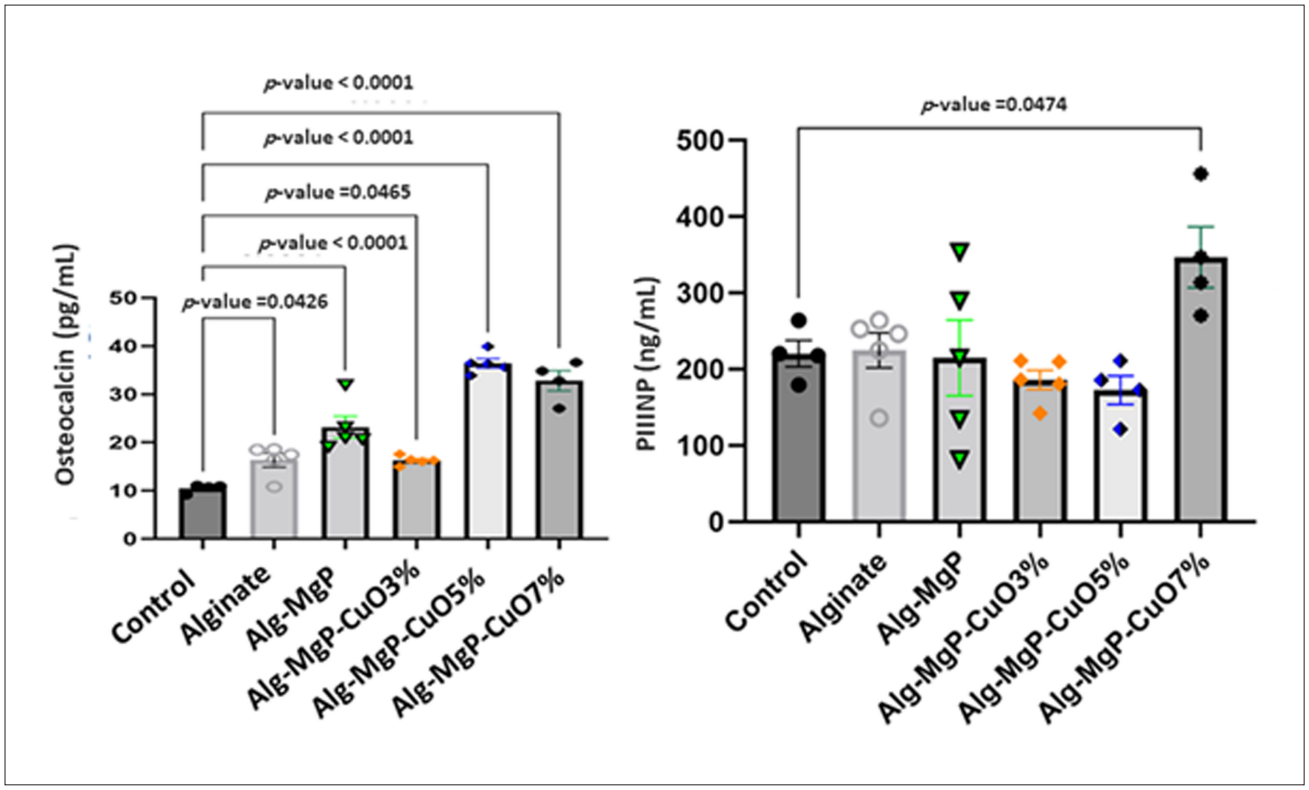

Figure 13. Serum osteocalcin (a) and procollagen III (PIIINP) (b) levels after filling the calvarial defects with the respective 3D scaffolds (n = 3).

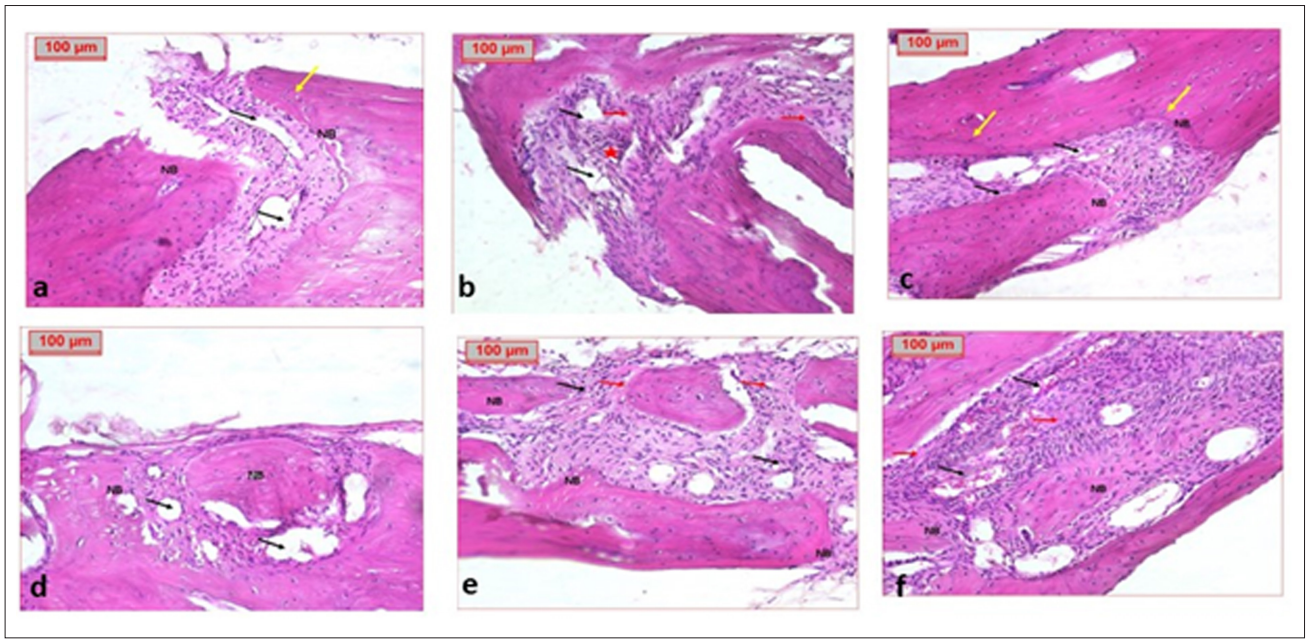

Figure 14. Hematoxylin and eosin (H&E) staining of XXX. (a) New bone formation and disconnected defect edges in control animals. (b) Granulation tissue (*), new blood vessels (black arrows), and fibrous tissue (red arrow) after Alg scaffold filling of the defect. (c) Defect treated with Alg–MgP scaffold revealed new bone formation at the defect edge (NB), a connected defect line (yellow arrows), and scattered blood vessels (black arrows). (d) Scaffold doped with 3% CuO induced regeneration at the boundary and within the defect area (NB), along with multiple scattered blood vessels (black arrows). (e) The 5% CuO scaffold displayed regeneration at the defect perimeter, fibrous tissue (red arrows), and scattered blood vessels (black arrows). (f) Scaffold doped with 7% CuO induced regeneration at the boundary of the defect (NB), and the tissue appeared highly vascular (black arrows). Magnification: 100×. Scale bars: 100 µm.

solutions. These materials possess low mechanical stability and only moderate biodegradability.[46,47] Although Ostim contains nanoscale apatite particles, its mechanical strength remains limited.[48,49,50] Bio-Oss Collagen® is a widely utilized bone graft that consists of a porous scaffold made of calcium and phosphorus. While it possesses the capacity for bone conduction, its capacity for promoting bone tissue regeneration is relatively poor.

Our 3D-printed scaffold demonstrated good mechanical strength due to the CuO dopant, consistent with previous studies incorporating inorganic metal oxides.[32,33,40] Additionally, the successful incorporation of MgP nanopowders into the Alg matrix enabled modulation of pore size and surface area, leading to enhanced porosity and surface area as indicated by adsorption isotherms. This tunability allows for customization of the scaffolds to meet optimal biological requirements.

Generally, materials that contain calcium or MgP are non-toxic, biocompatible, and bioresorbable. Magnesium offers an added advantage due to its ability to chelate various natural substances, supporting several metabolic processes.[43] This property can eliminate the need for additional surgical interventions to remove implants.[23] Additionally, Miner-Oss/Collagen® demonstrated significant regenerative capabilities in a 6-mm rabbit calvaria critical-sized defect model. Maxresorb, a synthetic bioceramic containing calcium, demonstrated enhanced osteogenic effects and the formation of well-structured and vascularized bone tissue matrix after 16 weeks.[51,52]

In this study, a complete bone tissue with vascularization and a filled defect area was observed through tomographical and histological examinations after 8 weeks of grafting. Based on our findings, our matrix demonstrates a unique capacity to support the regeneration of bone tissue with superior structural and vascular characteristics within a shorter timeframe.[53,54] Furthermore, our bioink fully degraded upon neo-tissue formation—a significant improvement over other existing products, such as Norian SRS, a CaP-based granule. Norian SRS gradually degrades from the outermost to the innermost layers, which can lead to the persistence of residual material and the potential need for surgical removal after tissue regrowth.

Inorganic metal oxides, such as CuO, have been observed to facilitate endothelial cell proliferation and differentiation. It can promote angiogenesis through hypoxia and vascularization in newly formed tissue, thus accelerating the bone regeneration process.[22] Previous studies have highlighted the vital role of Cu in the regulation of the vascular endothelial growth factor, fibronectin, and fibroblastic growth factors,[54] all of which play fundamental roles in bone healing and vascularization.[55,58] Lin *et al.*[41] demonstrated that small amounts of $Cu_3(PO_4)_2$ positively impact osteogenesis and angiogenesis in bone marrow-derived mesenchymal stem cells. This finding aligns with our histological and tomographical analyses, which indicated that the scaffold containing 7% CuO exhibited the most enhanced bone filling and highest vascular tissue density. Furthermore, Cu particles possess antimicrobial characteristics that can help to combat early-stage localized infections,[16,59] as bacterial colonization is a common complication in surgical procedures.[60]

Bone defects treated with the 3D-bioprinted scaffolds demonstrated enhanced osteogenesis and vascularized tissue, especially when using the Alg–MgP–CuO7% scaffold. The formation of blood vessels that provide adequate blood supply is crucial for improving the nutrition of bone tissue, thereby promoting the survival of tissue-engineered bone and protecting it from ischaemia.[15,49,54] Osteocalcin is an integral part of the bone formation process; it is secreted within the bone microenvironment and facilitates hydroxyapatite crystal formation, bone mineralization, and calcium ion homeostasis.[61] Serum osteocalcin levels have been correlated with increases in BMD during treatment.[62,63] Our study revealed that plasma osteocalcin concentration correlated with the percentage of CuO in the scaffolds. Osteocalcin is synthesized through the carboxylation of glutamic acid residues in an aerobic process requiring a reducing agent. It is plausible that an optimal percentage of CuO acts as a catalyst in the reaction, enhancing the reduction process and facilitating osteocalcin formation. This hypothesis aligns with the observed early release patterns in our *in vitro* assays.

The repair and regeneration of bone injuries require the interaction between multiple growth factors and cytokines that facilitate extracellular matrix production. Initially composed of type I collagen, the extracellular matrix forms in the callus. This temporary cartilaginous structure is later remodeled into calcified bone through tightly regulated intercellular and intracellular signaling pathways.[61] The early expression of collagen is indicated through the PIIINP biomarker. In the present study, increased PIIINP levels were observed after scaffold implantation, peaking in animals treated with the 7% CuO-doped scaffolds, and corresponded with osteocalcin levels.

The observed increments in osteocalcin and PIIINP levels correlated with histological findings and improvements in BMD at skull defect sites, particularly following grafting with Alg–MgP–CuO5% and Alg–MgP–CuO7% scaffolds. Furthermore, the scaffold's surface topography facilitated the diffusion of nutrients and growth factors through surface pores, as confirmed by

SEM analysis and consistent with previous reports.[64–66] Structural analysis validated the effective integration of MgP and CuO-doped MgP nanopowders within the Alg/PEI matrix, highlighting the scaffolds' potential for tissue engineering applications. The presence of bioactive functional groups and the release of Cu ions were likely responsible for the enhanced cell growth and angiogenesis after scaffold grafting. Overall, the *in vivo* performance in a critical-sized cranial defect model in rats demonstrated promising therapeutic outcomes. Future studies should focus on quantitatively assessing the release kinetics of Cu ions and evaluating their long-term biological effects to fully understand the scaffolds' therapeutic potential.

5. Conclusion

This study represents a significant advancement in BTE through the development of a novel 3D scaffold composed of MgP, CuO, and Alg to treat calvarial bone defects in a Wistar rat model. The successful fabrication of Alg–MgP–CuO scaffolds via 3D bioprinting demonstrates the potential for designing customizable and precise scaffolds. The characterization results indicate that CuO doping enhances mechanical strength, biological activity, and angiogenic properties of the scaffold. At a doping concentration of 7% (w/w), *in vitro* analyses demonstrated high cell viability, indicating excellent biocompatibility and osteoinductive properties. In vivo evaluation further validated the scaffold's therapeutic efficacy, with significant improvements in bone regeneration and healing observed in the calvarial defect model. Microscopic and histological analyses provided extensive evidence of improved healing and bone growth. The study also emphasized the synergistic effect of MgP and CuO in promoting an environment conducive to bone healing and regeneration. These findings highlight the promising application of Alg–MgP–CuO scaffolds in BTE, offering a foundation for future studies and potential clinical applications. Overall, this study reinforces the significance of innovative biomaterials in overcoming the challenges of bone defect repair, ultimately contributing to improved therapeutic outcomes.

Acknowledgments

None.

Funding

This research was funded by the project "Composite Bioinks for 3D Bioprinting and Their Application in Bone Tissue Engineering," supported by the Academy of Scientific Research and Technology (ASRT) in Egypt. The authors acknowledge the financial support of the National Research Foundation (NRF) of South Africa under the SARChI Chair program (grant no. PPNT230823145247) awarded to Prof. Yahya Choonara.

Conflict of interest

The authors declare no conflict of interest.

Author contributions

Conceptualization: Mostafa Mabrouk, Pradeep Kumar, Yahya Choonara

Formal analysis: Shaimaa El-Shebiney, Sara A. M. El-Sayed, Mduduzi N. Sithole, Mashudu T. Mphaphuli

Funding acquisition: Mostafa Mabrouk, Yahya Choonara

Investigation: Shaimaa El-Shebiney, Sara A. M. El-Sayed, Mduduzi N. Sithole, Mashudu T. Mphaphuli

Methodology: Shaimaa El-Shebiney, Sara A. M. El-Sayed, Mduduzi N. Sithole, Mashudu T. Mphaphuli

Project administration: Mostafa Mabrouk, Yahya Choonara

Supervision: Mostafa Mabrouk, Pradeep Kumar, Yahya Choonara

Writing—original draft: Shaimaa El-Shebiney, Sara A. M. El-Sayed, Mduduzi N. Sithole, Mashudu T. Mphaphuli

Writing—review & editing: Mostafa Mabrouk, Pradeep Kumar, Yahya Choonara, Hanan H. Beherei

All authors have read and agreed to the published version of the manuscript.

Ethics approval and consent to participate

The study was conducted in line with the Declaration of Helsinki and approval was obtained from the Animal Care and Use Committee of the National Research Centre (approval no. 1311102022).

Consent for publication

Not applicable.

Availability of data

Data is available from the corresponding author upon reasonable request.

References

1. Allison DC, McIntyre JA, Ferro A, Brien E, Menendez LR. Bone grafting alternatives for cavitary defects in children. *Curr Orthop Pract*. 2013;24(3):267. doi: 10.1097/BCO.0b013e3182910f94.

2. Chinnasami H, Dey MK, Devireddy R. Three-dimensional scaffolds for bone tissue engineering. *Bioengineering*. 2023;10(7):759. doi: 10.3390/bioengineering10070759.

3. Ren J, Jiang Y, Jin X, *et al*. Dissolution and intrusion of chloride disrupted biodegradation products to persistently accelerate biodegradation of Fe-based implants. *Corros Sci*. 2024;240:112461. ISSN 0010-938X. doi: 10.1016/j.corsci.2024.112461.

4. Jiang Y, Ren J, Jin X, *et al*. Accelerated biodegradation of Fe-30Mn-S biocomposite via preferential corrosion of secondary phase. *Intermetallics*. 2024;175:108539. ISSN 0966-9795. doi: 10.1016/j.intermet.2024.108539.

5. Micic M, Antonijevic D, Milutinovic-Smiljanic S, *et al*. Developing a novel resorptive hydroxyapatite-based bone substitute for over-critical size defect reconstruction: physicochemical and biological characterization and proof of concept in segmental rabbit's ulna reconstruction. *Biomed Eng Biomed Technol*. 2020;65(4):491-505. doi: 10.1515/bmt-2019-0218.

6. Liu L, Shi G, Cui Y, *et al*. Individual construction of freeform-fabricated polycaprolactone scaffolds for osteogenesis. *Biomed Eng Biomed Techol*. 2017;62(5):467-479. doi: 10.1515/bmt-2016-0005.

7. Tohamy KM, Soliman IE, Mabrouk M, *et al*. Novel polysaccharide hybrid scaffold loaded with hydroxyapatite: fabrication, bioactivity, and in vivo study. *Mater Sci Eng C*. 2018;93:1-11. doi: 10.1016/j.msec.2018.07.054

8. Ke D, Bose S. Effects of pore distribution and chemistry on physical, mechanical, and biological properties of tricalcium phosphate scaffolds by binder-jet 3D printing. *Addit Manuf*. 2018;22:111-117. doi: 10.1016/j.addma.2018.04.020.

9. Mabrouk M, Beherei HH, ElShebiney S, Tanaka M. Newly developed controlled release subcutaneous formulation for tramadol hydrochloride. *Saudi Pharm J*. 2018; 26(4):585-592. doi: 10.1016/j.jsps.2018.01.014.

10. Rakovsky A, Gotman I, Rabkin E, Gutmanas EY. β-TCP–polylactide composite scaffolds with high strength and enhanced permeability prepared by a modified salt leaching method. *J Mech Behav Biomed Mater*. 2014;32:89-98. doi: 10.1016/j.jmbbm.2013.12.022.

11. Błaszczyk B., Kaspera W., Ficek K., *et al*., Effects of polylactide copolymer implants and platelet-rich plasma on bone regeneration within a large calvarial defect in sheep. *BioMed Res Int*. 2018;2018(1):1-11. doi: 10.1155/2018/4120471.

12. Hasnain MS, Nayak AK. Alginates: *Versatile Polymers in Biomedical Applications and Therapeutics*. CRC Press; 2019.

13. Abbas HA, Mabrouk M, Soliman AA, Beherei HH. Dual-function membranes based on alginate/methyl cellulose composite for control drug release and proliferation enhancement of fibroblast cells. *Int J Biol Macromol*. 2020;164:2831-2841. doi: 10.1016/j.ijbiomac.2020.08.171

14. Tomić SL, Babić Radić MM, Vuković JS, Filipović VV, Nikodinovic-Runic J, Vukomanović M. Alginate-based hydrogels and scaffolds for biomedical applications. *Mar Drugs*. 2023;21(3):177. doi: 10.3390/md21030177.

15. Tohamy KM, Mabrouk M, Soliman IE, Beherei HH, Aboelnasr MA. Novel alginate/hydroxyethyl cellulose/hydroxyapatite composite scaffold for bone regeneration: In vitro cell viability and proliferation of human mesenchymal stem cells. *Int J Biol Macromol*. 2018;112:448-460. doi: 10.1016/j.ijbiomac.2018.01.181

16. Gutierrez E, Burdiles PA, Quero F, Palma P, Olate-Moya F, Palza H. 3D printing of antimicrobial alginate/bacterial-cellulose composite hydrogels by incorporating copper nanostructures. *ACS Biomater Sci Eng*. 2019;5(11):6290-6299. doi: 10.1021/acsbiomaterials.9b01048.

17. El-Sayed SAM, ElShebiney S, Beherei HH, Kumar P, Choonara YE, Mabrouk M. Copper-doped magnesium phosphate nanopowders for critical size calvarial bone defect intervention. *J Biomed Mater Res B Appl Biomater*. 2024;112(2):e35376. doi: 10.1002/jbm.b.35376.

18. Sithole MN, Kumar P, Du Toit LC, Erlwanger KH, Ubanako PN, Choonara YE. A 3D-printed biomaterial scaffold reinforced with inorganic fillers for bone tissue engineering: in vitro assessment and in vivo animal studies. *Int J Mol Sci*. 2023;24(8):7611. doi: 10.3390/ijms24087611

19. Mabrouk M, Mousa SM, ElGhany WAA, Abo-elfadl MT, El-Bassyouni GT. Bioactivity and cell viability of Ag+- and Zr4+-co-doped biphasic calcium phosphate. *Appl Phys A*. 2021;127(12):948. doi: 10.1007/s00339-021-05051-1.

20. Khalef L, Lydia R, Filicia K, Moussa B. Cell viability and cytotoxicity assays: biochemical elements and cellular compartments. *Cell Biochem Funct*. 2024;42(3):e4007. doi: 10.1002/cbf.4007

21. Tajik S, Garcia CN, Gillooley S, Tayebi L. 3D printing of hybrid-hydrogel materials for tissue engineering: a critical review. *Regen Eng Transl Med*. 2023;9(1):29-41. doi: 10.1007/s40883-022-00267-w. Epub 2022 Aug 1. PMID: 37193257; PMCID: PMC10181842.

22. Badawi MS, Elfayomy S, Zaki BM, Sayed AM, Abuzahra F. Assessment of healing in calvarial bone defect by allogenic demineralized bone matrix and adipose derived stem cells. *Egypt J Plast Reconstr Surg*. 2018;42(2):353-362. doi: 10.21608/ejprs.2018.80752.

23. Hohenbild F, Arango Ospina M, Schmitz SI, Moghaddam A, Boccaccini AR, Westhauser F. An in vitro evaluation of the biological and osteogenic properties of magnesium-doped bioactive glasses for application in bone tissue engineering. *Int J Mol Sci*. 2021;22(23):12703. doi: 10.3390/ijms222312703.

24. Dong J, Ding H, Wang Q, Wang L. A 3D-printed scaffold for repairing bone defects. *Polymers*. 2024;16(5):706. doi: 10.3390/polym16050706.

25. Dong Q, Zhang M, Zhou X, *et al*. 3D-printed Mg-incorporated PCL-based scaffolds: a promising approach for bone healing. *Mater Sci Eng C*. 2021;129:112372. doi: 10.1016/j.msec.2021.112372.

26. Mácová P, Viani A. Investigation of setting reaction in magnesium potassium phosphate ceramics with time resolved infrared spectroscopy. *Mater Lett*. 2017;205:62-66. doi: 10.1016/j.matlet.2017.06.063.

27. Stefov V, Šoptrajanov B, Kuzmanovski I, Lutz HD, Engelen B. Infrared and Raman spectra of magnesium ammonium phosphate hexahydrate (struvite) and its isomorphous analogues. III. Spectra of protiated and partially deuterated magnesium ammonium phosphate hexahydrate. *J Mol Struct*. 2005;752(1-3):60-67. doi: 10.1016/j.molstruc.2005.05.040.

28. Aramendía MA, Borau V, Jiménez C, Marinas JM, Romero FJ. Synthesis and characterization of magnesium phosphates and their catalytic properties in the conversion of 2-hexanol. *J Colloid Interface Sci*. 1999;217(2):288-298. doi: 10.1006/jcis.1999.6380.

29. Kanellopoulos A, Qureshi TS, Al-Tabbaa A. Glass encapsulated minerals for self-healing in cement based composites. *Constr Build Mater*. 2015;98:780-791. doi: 10.1016/j.conbuildmat.2015.08.127.

30. Zhao M, Du J, Lei H, *et al*. Enhanced electrocatalytic activity of FeNi alloy quantum dot-decorated cobalt carbonate hydroxide nanosword arrays for effective overall water splitting. *Nanoscale*. 2022;14(8):3191-3199. doi: 10.1039/D1NR08035K.

31. Fais G, Sidorowicz A, Perra G, *et al*., Cytotoxic effects of ZnO and Ag nanoparticles synthesized in microalgae extracts on PC12 cells. *Mar Drugs*. 2024;22(12):549. doi: 10.3390/md22120549.

32. Shen J-N, Yu C-C, Zeng G-N, Van der Bruggen B. Preparation of a facilitated transport membrane composed of carboxymethyl chitosan and polyethylenimine for CO2/N2 separation. *Int J Mol Sci*. 2013;14(2):3621-3638. doi: 10.3390/ijms14023621.

33. Pascual-González C, de la Vega J, Thompson C, *et al*. Processing and mechanical properties of novel biodegradable poly-lactic acid/Zn 3D printed scaffolds for application in tissue regeneration. *J Mech Behav Biomed Mater*. 2022;132:105290. doi: 10.1016/j.jmbbm.2022.105290.

34. Radhakrishnan S, Nagarajan S, Belaid H, *et al*. Fabrication of 3D printed antimicrobial polycaprolactone scaffolds for tissue engineering applications. *Mater Sci Eng C*. 2021;118:111525. doi: 10.1016/j.msec.2020.111525.

35. Liao M, Zhu S, Guo A, *et al*. 3D printed bioactive glasses porous scaffolds with high strength for the repair of long-bone segmental defects. *Compos B Eng*. 2023;254:110582. doi: 10.1016/j.compositesb.2023.110582.

36. Lei B, Gao X, Zhang R, Yi X, Zhou Q. In situ magnesium phosphate/polycaprolactone 3D-printed scaffold induce bone regeneration in rabbit maxillofacial bone defect model. *Mater Des*. 2022;215:110477. doi: 10.1016/j.matdes.2022.110477.

37. Sing KSW. Reporting physisorption data for gas/solid systems with special reference to the determination of surface area and porosity (Recommendations 1984). *Pure Appl Chem*. 1985;57(4):603-619. doi: 10.1351/pac198557040603.

38. Lowell S, Shields JE, Thomas MA, Thommes M. *Characterization of Porous Solids and Powders: Surface Area, Pore Size and Density*. Springer Science & Business Media; 2012.

39. Zhao XS, Lu GQ (Max), Millar GJ. Advances in mesoporous molecular sieve MCM-41. *Ind Eng Chem Res*. 1996;35(7):2075-2090. doi: 10.1021/ie950702a.

40. Broekhoff JCP. Mesopore determination from nitrogen sorption isotherms: fundamentals, scope, limitations. In: *Studies in Surface Science and Catalysis*. Elsevier; 1979;3:663-684. https://www.sciencedirect.com/science/article/pii/S0167299109602433. Accessed December 25, 2024.

41. Lin Z, Cao Y, Zou J, *et al*. Improved osteogenesis and angiogenesis of a novel copper ions doped calcium phosphate cement. *Mater Sci Eng C*. 2020;114:111032. doi: 10.1016/j.msec.2020.111032.

42. Yu W, Sun T-W, Ding Z, *et al*. Copper-doped mesoporous hydroxyapatite microspheres synthesized by a microwave-hydrothermal method using creatine phosphate as an organic phosphorus source: application in drug delivery and enhanced bone regeneration. *J Mater Chem B*. 2017;5(5):1039-1052. doi: 10.1039/C6TB02747D.

43. Noori A, Hoseinpour M, Kolivand S, *et al*. Exploring the various effects of Cu doping in hydroxyapatite nanoparticle. *Sci Rep*. 2024;14(1):3421. doi: 10.1038/s41598-024-53704-x.

44. Chen C-Y, Shie M-Y, Lee AK-X, Chou Y-T, Chiang C, Lin C-P. 3D-printed ginsenoside Rb1-loaded mesoporous calcium silicate/calcium sulfate scaffolds for inflammation inhibition and bone regeneration. *Biomedicines*. 2021;9(8):907. doi: 10.3390/biomedicines9080907

45. Jakus AE, Rutz AL, Jordan SW, *et al*. Hyperelastic "bone": a highly versatile, growth factor–free, osteoregenerative, scalable, and surgically friendly biomaterial. *Sci Transl Med*. 2016;8(358):358ra127-358ra127.

doi: 10.1126/scitranslmed.aaf7704.

46. Reginster J-Y, Seeman E, De Vernejoul MC, *et al*. Strontium ranelate reduces the risk of nonvertebral fractures in postmenopausal women with osteoporosis: treatment of peripheral osteoporosis (TROPOS) study. *J Clin Endocrinol Metab*. 2005;90(5):2816-2822.
doi: 10.1210/jc.2004-1774

47. Kazakova G, Safronova T, Golubchikov D, Shevtsova O, Rau JV. Resorbable Mg2+-containing phosphates for bone tissue repair. *Materials*. 2021;14(17):4857.
doi: 10.3390/ma14174857.

48. Patel H, Bonde M, Srinivasan G. Biodegradable polymer scaffold for tissue engineering. *Trends Biomater Artif Organs*. 2011;25(1):20-29.

49. Wu Z, Meng Z, Wu Q, *et al*. Biomimetic and osteogenic 3D silk fibroin composite scaffolds with nano MgO and mineralized hydroxyapatite for bone regeneration. *J Tissue Eng*. 2020;11:2041731420967791.
doi: 10.1177/2041731420967791.

50. Huber F-X, Belyaev O, Hillmeier J, *et al*. First histological observations on the incorporation of a novel nanocrystalline hydroxyapatite paste OSTIM® in human cancellous bone. *BMC Musculoskelet Disord*. 2006;7(1):50.
doi: 10.1186/1471-2474-7-50.

51. Garcia C, Orozco Y, Betancur A, *et al*. Fabrication of polycaprolactone/calcium phosphates hybrid scaffolds impregnated with plant extracts using 3D printing for potential bone regeneration. *Heliyon*. 2023;9(2):e13176.
doi: 10.1016/j.heliyon.2023.e13176.

52. Cheon E, Kim S-H, Lee D-K, *et al*. Osteostimulating ability of β-tricalcium phosphate/collagen composite as a practical bone-grafting substitute: in vitro and in vivo comparison study with commercial one. *Biotechnol Bioprocess Eng*. 2021;26(6):923-932.
doi: 10.1007/s12257-021-0059-4.

53. Kamal M, Andersson L, Tolba R, *et al*. Bone regeneration using composite non-demineralized xenogenic dentin with beta-tricalcium phosphate in experimental alveolar cleft repair in a rabbit model. *J Transl Med*. 2017;15(1):263.
doi: 10.1186/s12967-017-1369-3.

54. Potres Z, Deshpande S, Klöeppel H, Voss K, Klineberg I. Assisted wound healing and vertical bone regeneration with simultaneous implant placement: a histologic pilot study. *Int J Oral Maxillofac Implants* 2016;31(1):45-54.
doi: 10.11607/jomi.3951.

55. Luo R, Huang Y, Yuan X, *et al*. Controlled co-delivery system of magnesium and lanthanum ions for vascularized bone regeneration. *Biomed Mater*. 2021;16(6):065024.
doi: 10.1088/1748-605X/ac2886.

56. Wang Z, Zheng B, Yu X, *et al*. Promoting neurovascularized bone regeneration with a novel 3D printed inorganic-organic magnesium silicate/PLA composite scaffold. *Int J Biol Macromol*. 2024;277:134185.
doi: 10.1016/j.ijbiomac.2024.134185.

57. Stein GS, Lian JB. Molecular mechanisms mediating proliferation/differentiation interrelationships during progressive development of the osteoblast phenotype. *Endocr Rev*. 1993;14(4):424-442.
doi: 10.1210/edrv-14-4-424

58. Sousa CP, Dias IR, Lopez-Peña M, *et al*. Bone turnover markers for early detection of fracture healing disturbances: a review of the scientific literature. *An Acad Bras Ciênc*. 2015;87:1049-1061.
doi: 10.1590/0001-3765201520150008

59. Barralet J, Gbureck U, Habibovic P, Vorndran E, Gerard C, Doillon CJ. Angiogenesis in calcium phosphate scaffolds by inorganic copper ion release. *Tissue Eng Part A*. 2009;15(7):1601-1609.
doi: 10.1089/ten.tea.2007.0370.

60. Liu Y, Xu Z, Qiao M, Cai H, Zhu Z. Metal-based nano-delivery platform for treating bone disease and regeneration. *Front Chem*. 2022;10:955993.
doi: 10.3389/fchem.2022.955993.

61. Mostofi M, Mostofi F, Hosseini S, *et al*. Efficient three-dimensional (3D) human bone differentiation on quercetin-functionalized isotropic nano-architecture chitinous patterns of cockroach wings. *Int J Biol Macromol.* 2024;258(2):129155.
doi: 10.1016/j.ijbiomac.2023.129155

62. Hajduga MB, Bobiński R, Dutka M, *et al*. Analysis of the antibacterial properties of polycaprolactone modified with graphene, bioglass and zinc-doped bioglass. *Acta Bioeng Biomech*. 2021;23(10.37190):131-138.
doi: 10.37190/abb-01766-2020-03.

63. Zoch ML, Clemens TL, Riddle RC. New insights into the biology of osteocalcin. *Bone*. 2016;82:42-49.
doi: 10.1016/j.bone.2015.05.046.

64. Alarcin E, Akguner ZP, Ozturk AB, *et al*. Biomimetic 3D bioprinted bilayer GelMA scaffolds for the delivery of BMP-2 and VEGF exogenous growth factors to promote vascularized bone regeneration in a calvarial defect model in vivo. *Int J Biol Macromol*. 2025; 306(2):141440.
doi: 10.1016/j.ijbiomac.2025.141440

65. Dirckx N, Moorer MC, Clemens TL, Riddle RC. The role of osteoblasts in energy homeostasis. *Nat Rev Endocrinol*. 2019;15(11):651-665.
doi: 10.1038/s41574-019-0246-y

66. Kurdy NMG. Serology of abnormal fracture healing: the role of PIIINP, PICP, and BsALP. *J Orthop Trauma*. 2000;14(1):48-53.
doi: 10.1097/00005131-200001000-00010